THE UNIVERSITY OF QUEENSLAND

Bachelor of Engineering Thesis

Simulation of CubeSat Re-Entry Trajectory

Student Name: Steven APIRANA

Course Code: MECH4500

Supervisor: Professor Richard Morgan

Submission date: 2 June 2017

A thesis submitted in partial fulfilment of the requirements of the Bachelor of Engineering degree in Bachelor of Engineering Degree in Mechanical Engineering

UQ Engineering

Faculty of Engineering, Architecture and Information Technology

Abstract

Von Karman Institute in partnership with Ecole Centrale Paris are launching the QB50 program, comprising 50 CubeSats capable of performing scientific experiments in the thermosphere. One of these Cubesats, QARMAN, is designed to make measurements of ablation to inform the design of thermal protection systems for re-entry vehicles.

QARMAN will deploy a passive braking system upon re-entry to the atmosphere and peak-heating is expected to occur at an altitude of 50km. This was the design point for trajectory modelling. The re-entry velocity was determined to be in the range of 7.5 – 7.57km/s. The resulting velocity at peak-heating was found to be 6.35km/s using the lower bound of the entry velocity range.

A computational model was built to simulate the flow conditions over QARMAN during peak heating. The compressible flow code, eilmer3, was used and a 2D model was built subject to simplifying assumptions of the geometry of QARMAN. Bow-shock, boundary layer, and oblique-shock interactions were observed, and the boundary layer displacement thickness was measured to be 6.89mm at a distance 340mm downstream of the nose. A shock stand-off distance, influenced by boundary layer propagation, was observed, and measured to be 52.8mm upstream of the interface of fore-body and wedge-tip. This represents a stand-off distance that is 7.66 times the displacement thickness which is significantly larger than the commonly used 4x multiplier.

A 3:10 scaled-model of QARMAN was designed and built. A recess within the model allows for gauges to measure heat data, and the location of 8 holes to house thin-film gauges has been outlines. Two additional mounting pieces were designed and built to hold the model in the test section and these can be used for mounting other models.

An experiment has been designed for The University of Queensland's X2 expansion tube. The post-shock density was found and binary scaling was used to determine an appropriate driver gas configuration. Analytical calculation of the boundary layer thickness was compared with the CFD output and a difference between their predicted shock stand-off distances was found. The positioning of sensors was designed to capture this region of interest and comparison between experiments, CFD, and analytical predictions is recommended.

Acknowledgements

Thank you to Professor Richard Morgan for your supervision throughout this thesis. I am very grateful for the opportunity to conduct such interesting research. Thank you to Chris James for your regular advice and constant support throughout the project, and for proposing this thesis topic.

And thanks to my wife, Rebecca.

Contents

List of Tables

List of Figures

1. Introduction

1.1 Background

CubeSats provide a space rated platform that can be cheaply mounted on many rockets making it much cheaper and easier to fly a payload. The distribution of mass within the CubeSat and the potential for vibrating parts are some of the necessary considerations for joining a launch.

In 1999 Jordi Puig-Suari of California Polytechnic State University and Bob Twigg of Stanford University developed the initial specifications for CubeSats [1]. Given the geometric constraint of a 10cm cube, and a mass limit of 1.33kg, CubeSats were intended to perform scientific research in Low Earth Orbit (LEO) and to investigate new technologies. By 2015, hundreds of CubeSats had been launched, for University experiments, for Civilian exploration, and for Communication and Military purposes [1]. Clearly, enthusiasm for CubeSats has outstripped expectation.

The QB50 mission led by Von Karman Institute (VKI) proposes a network of 50 double CubeSats capable of performing "first-class science in the largely unexplored thermosphere" [2]. Within this group, the QubeSat for Aerothermodynamic Research and Measurement on Ablation (QARMAN) platform has been proposed as a "testbed for re-entry technologies" [3]. The proposed QARMAN re-entry CubeSat comprises an extra unit which contains the Thermal Protection System (TPS) and additional payloads [4]. QARMAN will be jettisoned from the International Space Station (ISS) and is intended to achieve a low energy re-entry at 7.5km/s [3]. It was expected that no CubeSat of the QB50 program would survive below 90 km, however the TPS is proposed to extend the survivability of QARMAN to an "end of life altitude of 50km" [3].

Atmospheric re-entry poses tremendous engineering challenges in surviving large g-forces for LEO return, and radiative heating on vehicle surfaces, particularly the nose. The TPS is critical for surviving the aerothermodynamic heating in the radiating shock layer [5]. The TPS of re-entry vehicles undergo tremendous radiative heating and can experience a range of high-temperature phenomena such as thermochemical ablation [6].

The importance of heat shield design is perhaps best illustrated by the before and after graphic of the Galileo heat shield (***Figure 1***).

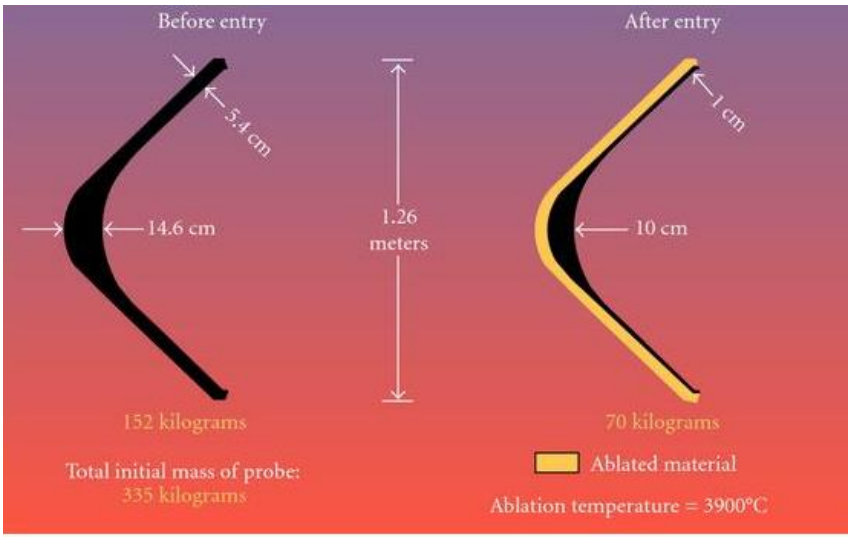

Figure 1: Galileo Heat Shield Ablation

Initial modelling for Galileo accurately predicted that the largest heating would occur at the nose and the resulting TPS accounted for this with increased thickness. As seen in *Figure **1***, ablation was over-predicted at the nose and under predicted on the flank, and a discrepancy between modelling and real-world results was identified. Since the TPS often accounts for a large fraction of total mass, the accurate replication of re-entry conditions is vital for optimising design and minimising wasted mass. Safety factors may be expected to drop with a reduction in mass, however an accurate analysis of ablation could inform the redistribution of mass to produce higher safety factors. These factors form the motivation for this research.

1.2 Thesis Goals

This research will investigate the hypervelocity flow properties and resulting high temperatures likely to be experienced by QARMAN during re-entry. A numerical trajectory model will be used to identify the flight-path angle and velocity magnitude of QARMAN upon re-entering the atmosphere. These re-entry conditions will be estimated using the ISS' initial altitude and inclination of 415km and 51.6 degrees respectively.

Trajectory data will be used to determine the flow conditions across QARMAN during re-entry.

The flow condition will be simulated using Computational Fluid Dynamics (CFD) in UQ's local in-house compressible flow code, eilmer3. This will provide a validation/check for experimental results, as well as potential validation of flight data.

An experiment has been planned for UQ's X2 expansion tube. In most cases, it is not possible to put full-scale models in the test section and binary scaling is used to replicate the flight velocity and flight Reynolds number [7].

This thesis proposes to produce flow simulations, and data, for hyper-velocity planetary re-entry conditions, to inform the selection of ablative materials and future TPS design.

1.2.1 Goal 1

Goal 1 was to determine the trajectory of QARMAN so that the re-entry velocity and angle could be approximated given that they were not available in the public domain. Re-entry velocity was used to determine the trajectory point during which QARMAN will experience peak heating. Velocity, Mach number, and atmospheric conditions at the altitude of peak-heating informed the development of a computational model as well as the design of experiments.

1.2.2 Goal 2

Goal 2 was to develop a computational model of the flow over QARMAN using Computational Fluid Dynamics (CFD). The geometry of QARMAN includes a blunt body, a 'flat plate' fore-body, and a 15° wedge, which produce several interesting flow profiles. A bow-shock, a boundary layer, and an oblique-shock are predicted over the CubeSat and the development of a computational model offers a convenient way to measure flow properties where measurement on experiments are difficult or otherwise not possible.

1.2.3 Goal 3

Goal 3 was to build a scale-model of QARMAN. As a precursor to conducting experiments, a scaled-model must be designed and built. The model should accurately represent the geometry of QARMAN and accommodate housing instrumentation and wiring for data collection. The model must also be mounted within the test section of X2 and potential mounting capabilities should be considered.

1.2.4 Goal 4

Goal 4 was to design an experiment in X2. The flow conditions over QARMAN during peak-heating should be determined and these must be replicated for experiments. The experiment should be well defined to capture a region of interest and interesting flow interactions.

1.3 Thesis Contribution

This thesis proposes to help refine the development of TPS through accurate modelling of heat transfer. Validation of a computational model offers an inexpensive tool for measuring flow phenomena over QARMAN and the observed shock profiles should provide contrast to the proposed experiment. Temperature data can be compared with the 'real world' experiments of QARMAN to provide validation to their tests.

The proposed experiment should yield interesting data and this can be compared with the analytical and simulated results in this thesis.

1.4 Thesis Scope

Trajectory models can be complex, particularly upon re-entry into an atmosphere where drag and other effects must be considered. The model developed here investigated the re-entry velocity based on jettison from the International Space Station. The trajectory point information was then calculated using a known altitude of peak heating, and a more complex trajectory profile within the atmosphere was not needed.

The CFD models a 2D geometry projected through one of two planes of symmetry. 3D flow effects are present in the flow field. Perturbations at the edges of the model propagate

downstream towards the centreline and, for lower Mach numbers, this results in interactions around the centreline. Flow fields over the four rear wedges may also interact. Based on the geometry of QARMAN, this is expected to occur only in a small region near the front corners of the wedges, and measurement along the centreline is not expected to be affected. While a 3D model can capture these effects, it was considered too large in scope for this thesis and 2D simplifications were made for modelling.

The scaled-model includes a simplified nose profile. The more complex nose shape would have been difficult to model without specified measurements, and the added complexity would have added to machining time and cost.

Only one, of the four wedges, was designed and built for the model. The resulting model was therefore smaller, and easier to design and build. Additional wedges were not expected to affect the shock wave boundary layer interactions on the centreline greatly indicating that the model simplifications were reasonable.

Several experiments are possible for the developed model. As discussed in Section 1.1.2, a bow-shock, a boundary layer, and an oblique-shock are expected over QARMAN. The experiment designed in this thesis proposes to look only at the boundary layer propagation and interactions with the oblique-shock.

1.5 Thesis Structure

Chapter 2 presents the Literature review. Chapter 3 discusses the development of a trajectory model. Chapter 4 discusses the Computational Fluid Dynamics simulations. The model design and construction approach is outline in Chapter 5. An experiment was designed and this is discussed in Chapter 6.

2. Literature Review

Like most CubeSats, QARMAN has a simple geometry. The position and shape of QARMAN's TPS can be seen in *Figure **2***. Four deployable fins/solar cells act as a passive braking system to increase drag and to stabilise QARMAN once into Earth's atmosphere. The symmetry allows for further simplification in CFD simulations and scale-model design.

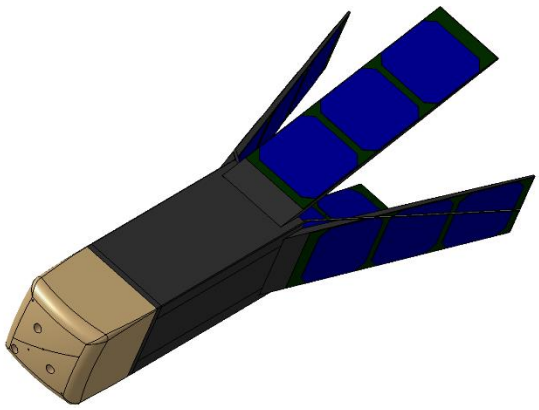

Figure 2: QARMAN [3]

The following literature review investigates approaches to trajectory modelling, building CFD simulations, and designing experiments to be conducted within The University of Queensland's X2 expansion tube.

2.1 Trajectory Modelling

In order to predict the flow conditions QARMAN will experience during re-entry, a trajectory model should be developed. Table **1** presents the geometry and mass of QARMAN which will be used in modelling. *Figure **3*** presents the Geometry of a typical atmospheric entry trajectory.

Table 1: QARMAN Geometry

Base platform	10 x 10cm cross-section	34cm in length
Stabilisation panels	10 x 34cm	15° inclination
Mass		5kg

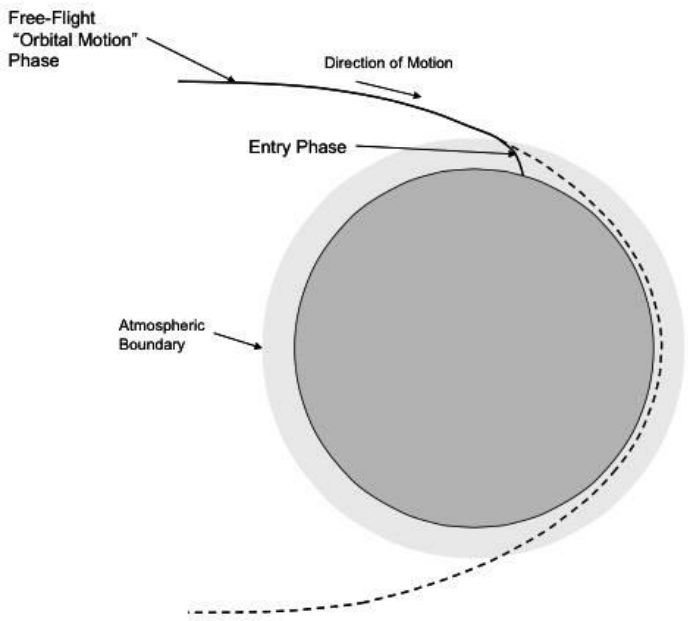

Figure 3: Typical Atmospheric Entry Trajectory [8]

There are numerous ways to design a re-entry trajectory. For this thesis, initial jettison conditions, – altitude, mass, and orbital velocity – have been provided and the entry conditions are to be determined numerically. One approach is to apply conservation of energy, and angular momentum equations. Hicks [8] describes a planar entry trajectory as "motion confined to the plane of a great circle" [8]. For their model, several simplifying assumptions are made which includes ignoring planetary rotation. For short entry phases, only a small amount of rotation occurs and this assumption is appropriate. For longer entry phases however, this may no longer be a reasonable assumption. Since QARMAN is expected to burn up in the atmosphere, the geographic location above earth is not required and the model can be applied.

In 1925 Walter Hohmann published a description of what is now known as the Hohmann transfer orbit [9]. The Hohmann transfer orbit describes an ellipse which joins two coplanar circular orbits of different radii (*Figure **4***). Hohmann's equations can describe the least amount of energy required to change from one circular orbit to another. While highly energy efficient, this is also typically a very slow way to change orbits. Given the goal of "low energy re-entry" at 7.5 km/s this more efficient approach is desirable.

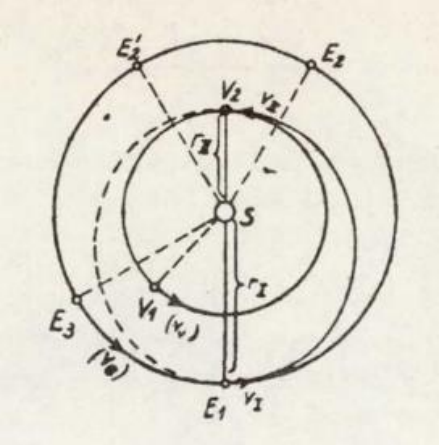

Figure 4: Hohmann Transfer [9]

The developed trajectory model is described further in Section 0. Once the re-entry trajectory has been determined, the flow conditions can be modelled using Computational Fluid Dynamics (CFD), and experimental re-creation within an expansion tube can be investigated.

2.2 Computational Simulations

Computational models can represent a significant reduction in time, cost, and difficulty often associated with conducting experiments. Data collection can be difficult during experiments, and a computational model offers a way to investigate flow properties where physical boundaries are prohibitive.

Numerical methods can be used to validate experimental results or, often, a computational model is validated through comparison with experiments. In the case of hypersonic flows, fluid dynamics assumptions apply to re-entry through the earth's atmosphere. Computational Fluid Dynamics (CFD) typically involves solving the Navier-Stokes equations [10]. These may be expressed as either incompressible, or compressible flow equations. Compressible flow assumptions allow for the change of a fluids density with the flow [11]. Given the re-entry condition, a change in fluid density is expected and compressible flow assumptions are applicable. UQ's local in-house compressible flow code, eilmer3, provides numerical solutions to the Navier-Stokes equations and is capable of modelling transient compressible flow in two and three spatial dimensions [12].

A 3D model is often necessary to accurately capture flow over complex geometries or for turbulent flows. Eilmer3 defines blocks in the 3D grid space by six surfaces [12]. The additional spatial dimension, means that a 3D mesh typically takes much longer to solve than a 2D mesh [12]. Given the simple geometry of QARMAN, a 2D model may be used to approximate conditions along a centreline for a limited distance along the nose. The reduction in complexity, and therefore reduction in computational effort, means shorter simulation times.

In addition to comparison with analytical solutions, the CFD model can be validated through comparison with experimental results.

2.3 X2 Expansion Tube

The University of Queensland first began hypersonic research in 1977 after the arrival of Professor Ray Stalker. The Australian Research Council (ARC) funded the development of a Reflected Shock Tunnel (RST) and it was Stalker's invention, the free-piston driver [13] that would theoretically allow the RST (T4), larger in scale than its predecessors T1, T2, and T3, to facilitate the test conditions (test times and stagnation pressure) needed to model hypersonic combustion and propulsion [14]. T4 began operation in 1987 [14] and would continue operation firing its 10,000th shot in 2008 [15]. RST were limited to sub-orbital flight-speeds due to the stagnation of test gasses upstream of the supersonic nozzle and in the late 1980s NASA Langley contracted the new hypersonics group at UQ to investigate higher enthalpy ground test possibilities.

The expansion tube, first proposed by Resler and Bloxom [16], could theoretically produce these higher enthalpy flow conditions. The two main difficulties with previous hypervelocity facilities were the extremely high reservoir temperatures and pressures, and the break-down in thermochemical equilibrium of gasses during expansion in the nozzle [17]. TQ (***Figure 5***) was set up as a pilot facility to investigate whether the versatility of the free-piston driver might expand the range of effective test conditions.

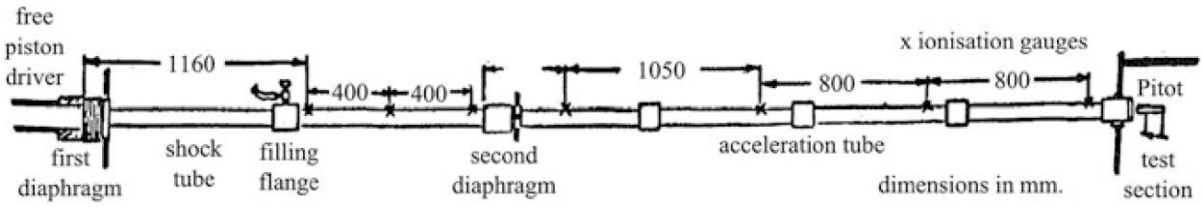

Figure 5: TQ experimental setup [16]

From earlier studies in NASAs Langley Expansion Tube/Tunnel it was found that only a narrow range of flow conditions were possible for a given test gas [17]. Studies with TQ would lead to the discovery of the cause of flow unsteadiness by Paull and Stalker [18], which would explain the mechanism behind the noise observed and facilitated the development of an expansion tunnel able to avoid this problem.

Shock tunnels add energy to a flow through shock waves, and for very high shock speeds this results in dissociation of the test gas. Expansion tubes use an additional low pressure tube. Part of the energy added to the flow comes from the shock wave and, after the initial shock has processed the test gas, an unsteady expansion processes the test gas. Thermal energy upstream of the shock is converted to velocity in the downstream gas. Pressure is the mechanism by which the energy is transferred and the result is a test gas that can be "cooling down as its velocity increases" [19]. In this way, at the expense of test time, the total enthalpy and total pressure are increased and the higher enthalpies applicable to planetary re-entry can be achieved.

Modification of TQ produced the X1 tunnel, and additional iterations have seen the construction of the X2 and X3, both successively larger tunnels built at UQ. This research proposes to use X2 to reproduce the flow conditions for QARMAN during re-entry into Earth's atmosphere.

Figure ***6*** presents a schematic diagram of a free-piston driven expansion tube alongside the wave processes which occur through the tunnel.

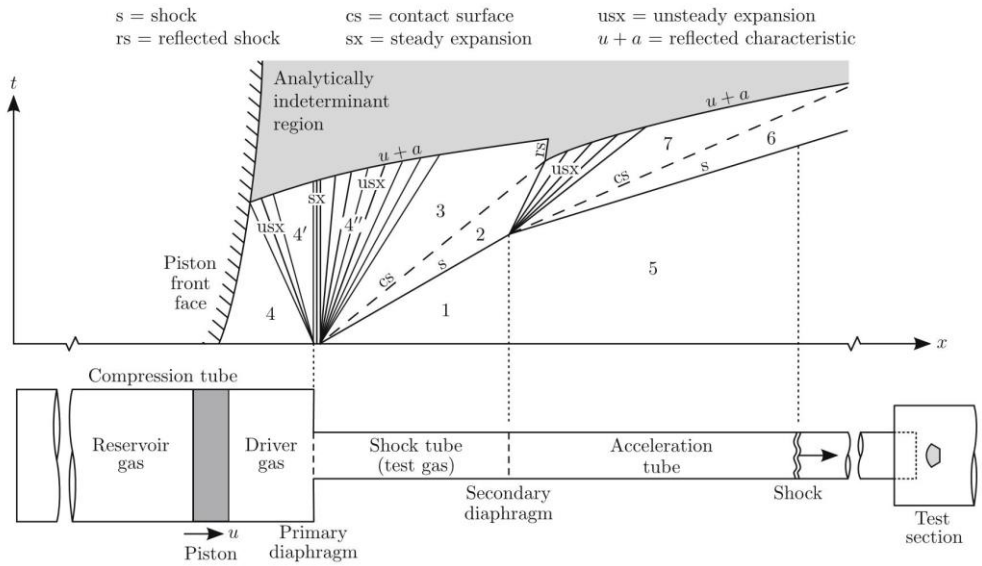

Figure 6: Schematic diagram of free-piston driven expansion tube [20]

During operation, the heavy piston is fired towards the primary diaphragm, the test gas (a light 'driver' gas such as helium) is compressively heated, and temperature and pressure increases until the gas explodes through the diaphragm. Fragments of this diaphragm can travel down the tube with the driver gas causing "significantly devastating results" [21] and research for improving the design of diaphragm systems has been conducted.

At the moment of rupture, the driver-gas pressure and temperature can be tens of Megapascals and thousands of Kelvin respectively. This drives an extremely strong shock into the test gas compressing and accelerating it down the tube [20]. The now high pressure and temperature test gas hits the second diaphragm (typically Mylar) and explodes through it into the low pressure of the acceleration tube. The sudden pressure difference allows the test gas to expand through the acceleration tube towards the test section from several km/s to speeds "as high as 20km/s [20]. This is the unsteady expansion process which gives the Expansion Tube its name.

The test gas is never stagnated, as it is in RST, and this removes the structural limits of total temperature and pressure. Not all of the test gas can be processed and this results in reduced test times. The test begins when the expanded test gas arrives at the test piece and ends when the downstream unsteady expansion wave arrives.

Prior to conducting experiments a full experimental procedure will be developed and this will be informed by these operational parameters.

2.4 Binary Scaling

The nose of QARMAN measures 100mm x 100mm which will fit within the test section and is smaller than the nozzle exit area (*Figure 7*). This does not, however, account for wall interactions and boundary layer propagation, or the fins at the back of QARMAN. Rather than the nozzle exit diameter, the core-flow diameter, which is the diameter of usable test gas, should be considered. These additional parameters make it necessary to build a scale model.

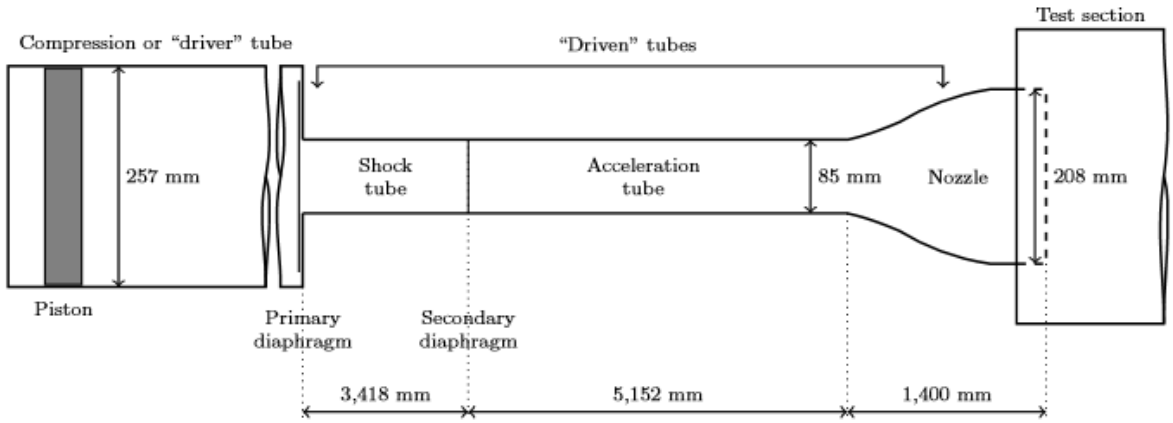

Figure 7: X2 expansion tube schematic in the most common configuration [19]

Binary scaling is usually used as it conserves the Reynolds number and binary reaction rates present in the non-equilibrium layer [22]. This approach is appropriate for chemical kinetics and conductive transfer but not always for radiative transfer [7]. The binary scaling parameter can be conserved by maintaining the product of density 'ρ' and a characteristic length 'L' [23].

2.5 Sensors

One method of collecting data from experiments is to use sensors attached to the model. Thin film sensors are often used for measuring surface temperature in hostile, high temperature environments [24]. Thin films are orders of magnitude thinner than wire and so produce less interactions with flows and less disruption of thermal patterns [24].

Thin film gauges are susceptible to damage if impacted by solid particles carried by a flow [25]. They can, however, provide temperature data throughout the duration of experiments (before and during) and these time histories are a significant counter-point to the disadvantage of gauge susceptibility to damage. Gauges can be clustered close together to give a better resolution of the thermal profile and correct techniques can provide data which is accurate to within 5-8% of the heat transfer rate [25]. Measurement of surface temperature histories '$T_s(t)$'enables surface heat transfer '$\dot{q}_s(t)$' to be computed using numerical techniques such as those used by Schultz and Jones (1973) and Oldfield and colleagues (1978) [26, 27].

On surfaces incident to the flow thermocouple gauges are preferred to thin-films as they are physically more durable and are often reparable. For data collection on a scaled-model of QARMAN, a combination of thermocouple and thin-film gauges may be required and this will be informed by further refinement of a region of interest for experiments.

3. Trajectory Modelling

3.1 Introduction

The trajectory model has been divided into two sections. The first, Section 3.2, investigates the potential re-entry velocity, 'V_E' of QARMAN upon entering Earth's atmosphere. Given that jettison is from the International Space Station, (ISS) the initial velocity and altitude were known. Within the atmosphere, much more complexity is involved in modelling a trajectory. Drag effects can no longer be ignored, and the free-stream temperature, pressure, and density will influence the flight trajectory. Bailet and colleagues have predicted that peak heating will occur at 50 km altitude [4]. This information, in conjunction with the re-entry velocity V_E, was used to develop the final trajectory information in Section 3.3.

3.2 Jettison Trajectory

A trajectory model has been developed using the following simplifying assumptions:

- A 2D coplanar, circular orbit approximation is appropriate for determining the re-entry velocity and flight-path angle.
- QARMAN is designed to burn up in the atmosphere at around 50km altitude [4] and as such, planetary rotation is not considered since the footprint on the planet is not required.

Conservation of Momentum and Energy equations were used in the development of a trajectory model. The Hohmann transfer method implements two impulses, the first to exit a current orbit, and the second to adjust to the new orbit. Since VKI is proposing for QARMAN to enter earth's atmosphere and apply a passive braking system, the second impulse is not required [4]. The velocity of a circular orbit was first calculated using Equation 1.

$$v_{circ} = \sqrt{\frac{\mu}{r}} \tag{1}$$

Here, 'r' is the circular orbit radius at an altitude of interest. Using a Hohmann transfer approach, Equation 2 calculates the required change in velocity 'Δv' to exit an orbit and enter an elliptical transfer orbit.

$$\Delta v = \sqrt{\frac{2\mu}{r_1} - \frac{2\mu}{r_1 + r_2}} - \sqrt{\frac{\mu}{r_1}} \tag{2}$$

Here 'r_1' is the radius to the ISS, 'r_2' is the radius to the re-entry point, and 'μ' is the standard gravitational parameter for Earth. *Figure* ***8*** presents the orbital model outline.

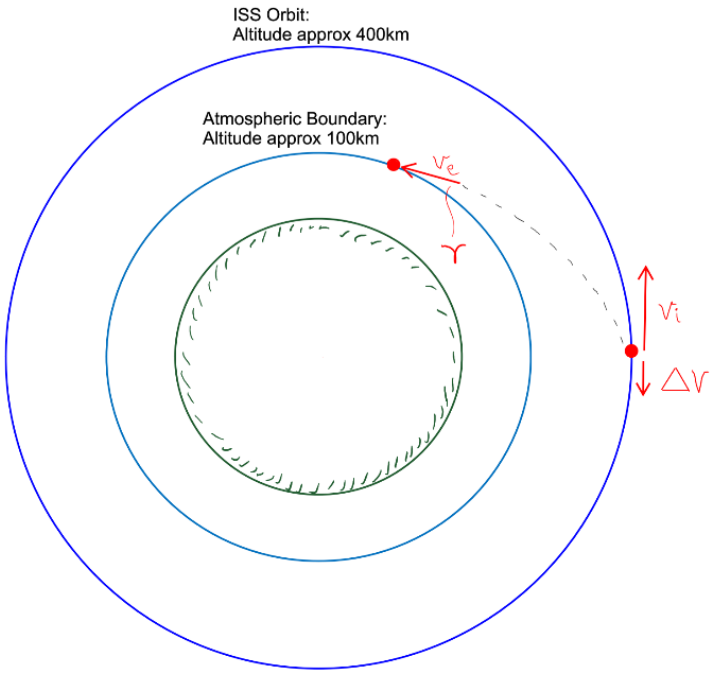

Figure 8: Atmospheric Entry Trajectory

The desired trajectory information is the re-entry flight-path angle 'γ' and the velocity magnitude 'V_e'. The model takes the ISS orbit as predominantly circular and given the eccentricity, e ≈ 1, this is an appropriate assumption. The applied Δv results in an elliptical orbit with its closest point being the atmospheric boundary (taken to be the Karman line, approximately 100km altitude), and its farthest point being the ISS altitude. The required Δv for this condition was found to be -91.46m/s, however it is acknowledged that this impulse would not result in atmospheric re-entry but rather QARMAN would brush the atmospheric boundary then depart again to complete the elliptic orbit.

Intuitively, larger deceleration is required to place QARMAN on a re-entry trajectory and 91.46m/s sets the lower bound for Δv.

The orbital velocity if the ISS is 7.66km/s and given the desired low energy re-entry at 7.5 km/s, 160m/s was selected as the upper bound for Δv. There is uncertainty regarding the initial jettison force however given the order of magnitude of the velocities, this is reasonably small.

3.3 Entry Angle and Velocity

From Bailet and colleagues the altitude at which peak heating occurs is known to be 50km [4]. Equation 3 can be used to determine this altitude analytically for a given re-entry angle.

$$y = \frac{1}{\beta}\, ln\left\{\frac{3C_D\rho_0 A}{\beta m \sin\theta_E}\right\} \tag{3}$$

Here 'β' is $\frac{1}{y_0}$; and 'y_0' is the characteristic height (6620m for Earth). 'A' is the cross-sectional area facing the flow, and ρ_0 is the free-stream density at the given altitude. Equation 3 makes 'flat-earth' approximations which, given the scale of the re-entry region, is a reasonable assumption. A drag coefficient, C_D, was estimated to be 2.05 and Equation 3 was then rearranged to calculate the re-entry angle, θ_E.

Equation 4 was used to determine the velocity at which peak heating will occur.

$$V_{PEAK} = V_{ENTRY} \times e^{\frac{-1}{6}} \tag{4}$$

Given the entry velocity range, 7.50 – 7.57 km/s, the resulting velocity range at peak heating will be 6.35 - 6.41 km/s. Equation 5 was then used to determine the Mach number for this velocity and altitude.

$$M = \frac{V}{a} \tag{5}$$

Where ‘a’ the sound speed at a given altitude, is determined using Equation 6.

$$a = \sqrt{\gamma RT} \tag{6}$$

3.4 Results

Table **2** presents the free-stream properties at 50km altitude, taken from U.S. Standard Atmosphere tables, and the resulting Mach number given the determined velocity.

Table 2: Free-stream properties at 50km altitude

Nomenclature	**Value**	**Description**
A	50	Altitude (km)
T∞	270	Temperature (K)
P∞	75.9	Pressure (Pa)
ρ∞	9.8E-4	Density (kg/m^3)
a	0.33	Sound Speed (km/s)
θ_E	8.1	Entry Angle (°)
V_{ENTRY}	7.5 – 7.57	Entry Velocity (km/s)
V_{PEAK}	6.35 – 6.41	Velocity at Peak Heating (km/s)
M	19.37 – 19.42	Mach no. at Peak Heating

These flow conditions, particularly Mach number, Velocity, Pressure, and Temperature, then formed the parameters for experimentation and computational simulations.

3.5 Summary

The trajectory point was selected to be the point of peak-heating. A Hohmann transfer approach was used to determine the minimum required Δv for re-entry, and the resulting re-entry angle and velocity at peak heating were calculated. An upper bound for re-entry velocity was chosen based on the desire for QARMAN to achieve low energy re-entry and this resulted in a range for Velocity and Mach number. All future calculations and simulations take the lower bound for these values.

4. Computational Fluid Dynamics

4.1 Introduction

This chapter discusses the development of a computational simulation, built using The University of Queensland's in-house compressible flow code, eilmer3. As discussed in Section 2.2 the benefits of a computational model include reductions in the time, cost, and difficulty often associated with conducting experiments. Data collection can be particularly difficult for experiments and this highlights the benefits of a validated CFD model. The model developed in this chapter is designed to complement the proposed experiment in Section 6.

The flow field is fully 3D, with two planes of symmetry (*Figure **9***). The 3D flow effects propagate in from the edges. Quasi-2D flow occurs until the perturbations reach the middle at which point 3D flow effects disrupt the flow along the centreline. The flow Mach number effects the rate of procession towards the centreline and for a sufficiently high Mach number a quasi-2D model is appropriate. The added complexity of a 3D model was time prohibitive in this case, but is proposed as future research.

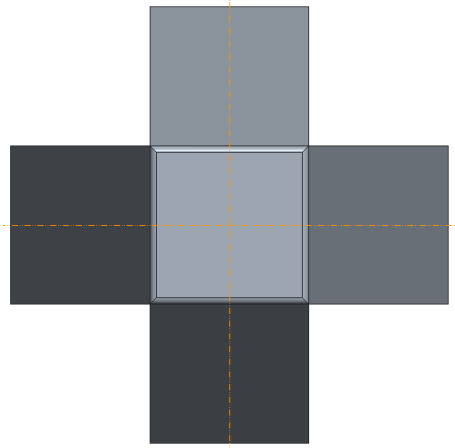

Figure 9: Planes of Symmetry

Section 4.2 discusses the computational domain and the blocking structure used to define the mesh. Section 4.3 discusses the clustering approach used to address skew issues within the grid. Investigation and optimisation of simulation run-time is presented in Section 4.4. Results of a grid-independence study are presented in Section 4.5. Discussion of results

is presented in Section 4.6 along with a deeper investigation into the influence of boundary layer propagation on the upstream shift of an oblique shock wave.

4.2 Blocking and Meshing

The blocking structure was built to capture the nose, upper surface, 15° wedge, and trailing wake of QARMAN. The nose was further simplified to match that of the physical model which is flat with a 2mm rounded edge (discussed in Section 5.2).

The domain was arranged to capture the bow shock, boundary layer, oblique shock, and some of the trailing wake behind QARMAN. *Figure **10*** presents the blocking structure used for simulations.

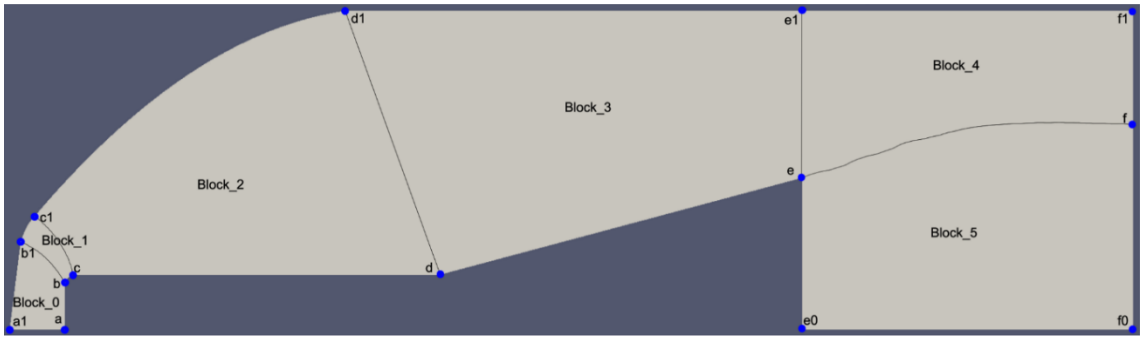

Figure 10: Block Structure

Early simulations included only Blocks 0, 1, and 2. As grid issues were resolved, more blocks were added incrementally; Block 3 to include the wedge; Blocks 4 and 5 to observe the trail. Simulations over the course mesh were used to modify the domain to better capture the shock profile and minimise unused grid space.

4.3 Clustering

It is typical that a flow simulation will have a particular Region of Interest (ROI). Clustering allows for the ‘bunching’ of grid cells, around specified ROI. *Figure **11*** and *Figure **12*** present the clustered nose profiles of the coarse and fine meshes respectively.

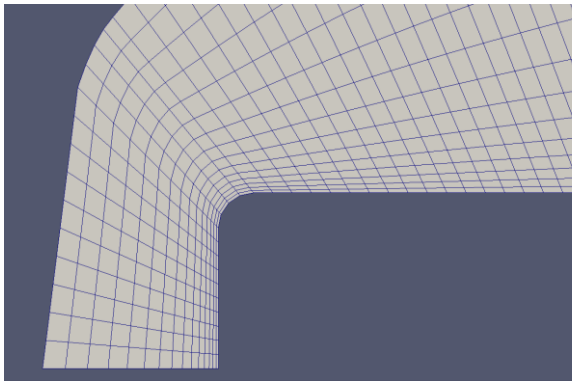

Figure 11: Clustered Coarse Mesh at the Nose

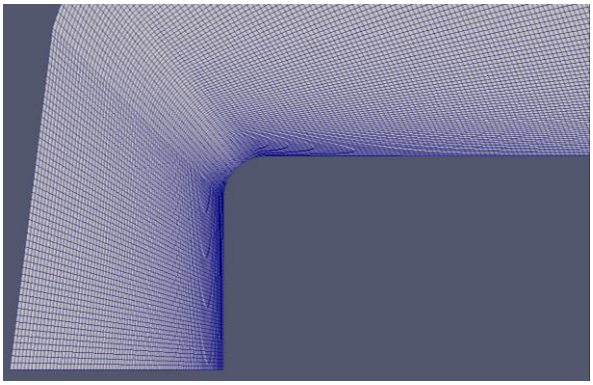

Figure 12: Clustered Fine Mesh at the Nose

The stagnation point on the surface of the vehicle experiences the maximum pressure [28]. Since the centre of the nose is where the stagnation point occurs, clustering was used to give more definition around that surface. An appropriate clustering strength was determined first using the coarse mesh (*Figure **11***). Higher fidelity meshes maintained a similar clustering strength with only minor alterations needed to address skewing issues (*Figure **12***).

The propagation of a boundary layer along the horizontal surface results in an oblique shock that stands before the wedge-tip rather than exactly at the tip (*Figure **21***). This is discussed further in Section 4.6.2. The area beneath the tip of the oblique shock, within the boundary layer, is the ROI for experiments and clustering was applied to give greater definition in that area. *Figure **13*** and *Figure **14*** present the clustered wedge profiles of the coarse and fine meshes respectively.

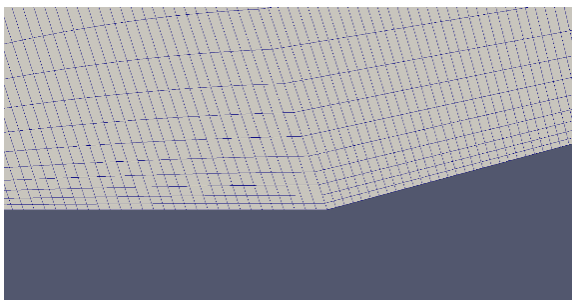

Figure 13: Clustered Coarse Mesh at the Wedge-tip

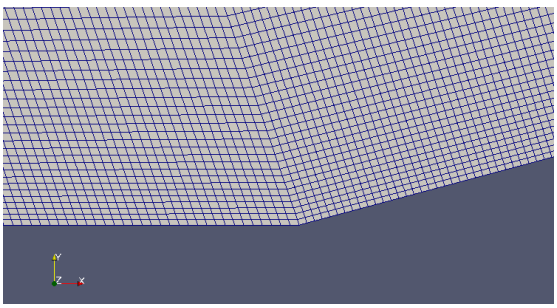

Figure 14: Clustered Fine Mesh at the Wedge-tip

As can be seen in *Figure **13***, there is some visible skew across the block boundary. Skew was not large enough in the coarse mesh to interrupt simulation solutions and this became less of an issue with increasingly higher fidelity simulations (*Figure **14***).

Roberts Cluster Functions were used for all clustering. The function allows the user to easily modify clustering strength and this was helpful when troubleshooting the mesh to solve skew issues.

4.4 Settling Time

As skew issues were addressed, higher fidelity simulations could be run. To ensure simulations did not run too long, early simulations were observed to investigate settling time. That is, how long before the flow reaches a steady-state and the flow effects can be interpreted accurately? Typically, a reasonable simulation time is the ratio of the model height and the flow velocity. This approach was used for early simulations and only very minor adjustments to time parameters were necessary. *Figure **15*** to *Figure **18*** presents pressure contours of the simulations from t = 0.00019s to t = 00040s.

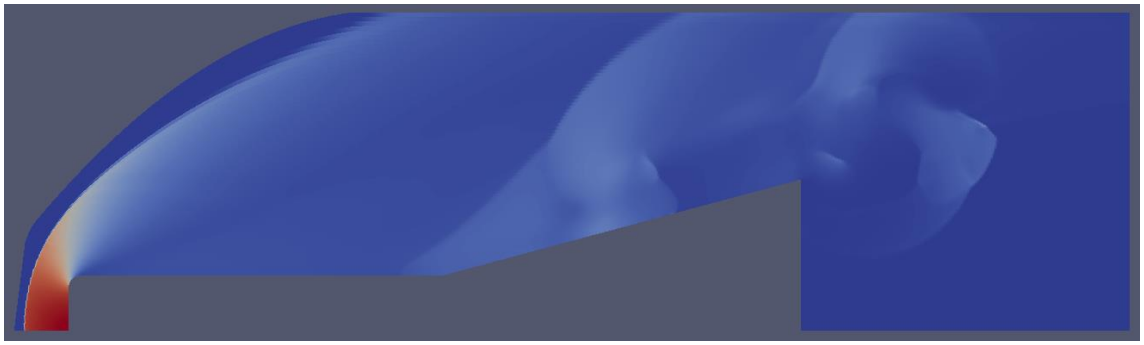

Figure 15: t = 0.00019s

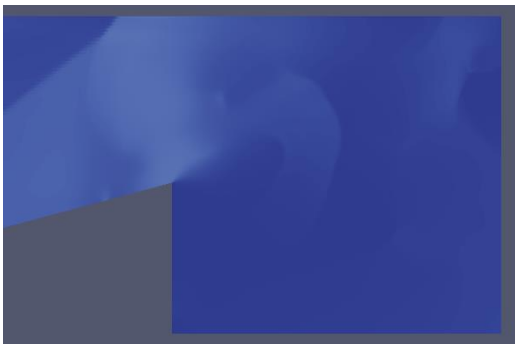

Figure 16: t = 0.00026s

Figure 17: t = 0.00033s

Figure 18: t = 0.00040s

At t = 0.00019 the simulation is approximately half way through. Vortices and eddies are still evident in the flow, particularly along the wedge and emerging into the wake. At t = 0.00026 the bulk of the flow upstream has settled and only some circulations are still present at the rear-tip of the wedge. At t = 0.00033 there are only very small sections in the wake which still need to settle. The flow has settled after t = 0.00040 and this run-time was applied to all higher fidelity simulations.

4.5 Grid Independence Study

Once the grid was discretised and the viscous solver was initialised it was necessary to determine that solutions were grid independent and to find the minimum required cell-count. This was performed by incrementally increasing the cell count, recording the value of a control variable at each iteration, and plotting the results to determine the settling point for that value. For this study, the pressures at the nose and at the wedge-tip were found for each increment.

The block-to-block cell count ratios, in the x-direction (parallel to the model surface), provided a basis for maintaining grid symmetry. Table **3** presents the Cell Counts (nnx) for each block of the coarse mesh.

Table 3: Coarse Mesh Grid Distribution

Block #	Cell Count (nnx)
0	15
1	10
2	4
3	60
4	75
5	60

An incremental multiplier was applied to the cell count for each block. While some additional modifications were required at higher discretisation, this provided a useful model.

Table 4 presents the results of the investigation into grid independence.

Table 4: Grid Independence Data

Cell Count	**Pressure at Node A** (pa)	**Pressure at Node D** (pa)	**CFL**	**Solve Time** (minutes)	**Machine**
6725	37854	3224	0.4	12	i7 4 Core CPU using e3shared
10800	36771	3019	0.4	23	
15680	36790	3027	0.4	42	
21520	36900	2983	0.4	72	
26800	36896	2945	0.4	92	
41350	36960	2955	0.7	122	
78260	36922	2904	0.8	44	i7 8 Core CPU using e3mpi
120400	36983	2943	0.9	196	

Two different machines were used to run simulations. For lower discretised meshes (<60,000 cells), a Microsoft Surface-Pro was used until solution times became too long (>300 minutes). More defined meshes were run on a Dell machine, with 8 cores and 16MB of RAM. For these simulations, the Message Passing Interface (MPI) of eilmer3 was used. This method assigns one MPI to each block of the mesh and, as can be seen in

Table 4, this resulted in a large reduction in simulation times.

The Courant-Friedrichs-Lewy condition (CFL) ensures that mesh discretisation and the simulation time-step are paired appropriately so that simulations converge to accurate solutions [29]. For lower cell counts, – larger individual cells – the CFL was kept at 0.4 (typically, a CFL of 0.5 is sufficiently small for simple simulations using eilmer3). For higher cell counts, – smaller individual cells – the CFL was increased incrementally and this helped to reduce solution times while maintaining the accuracy of simulations.

*Figure **19*** and *Figure **20*** present plots of pressure at the Nose and Wedge-tip respectively.

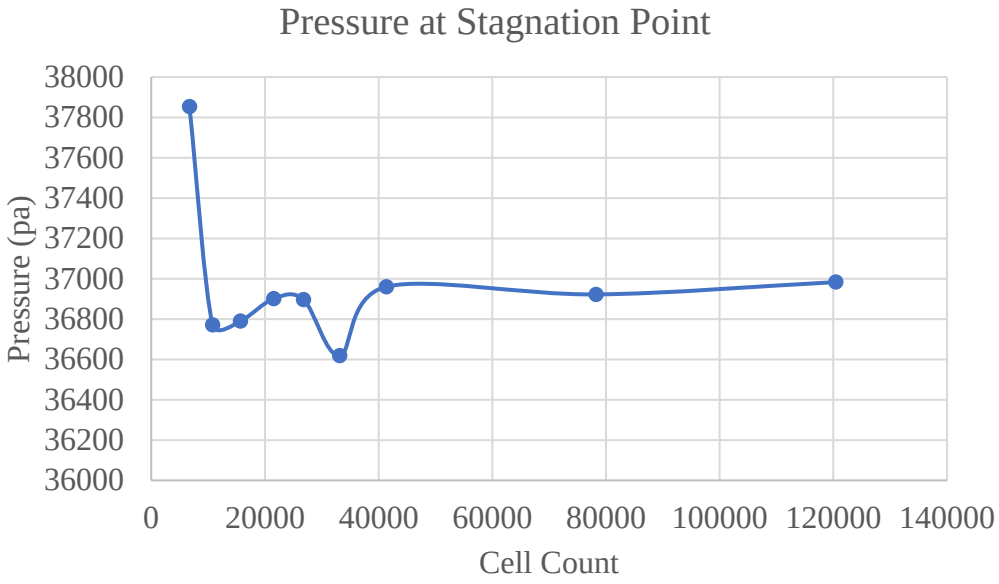

Figure 19: Grid Independence - Pressure at Stagnation Point

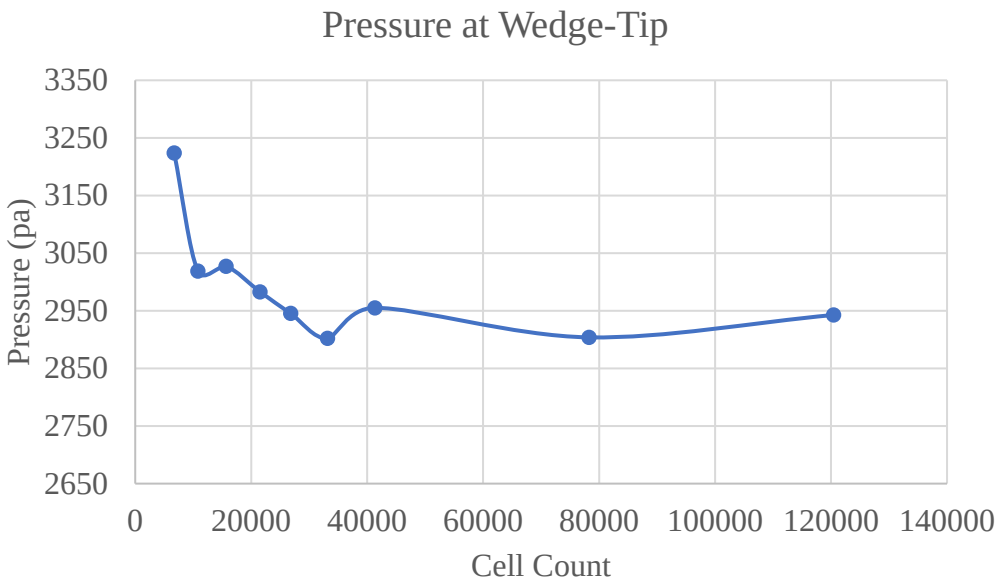

Figure 20: Grid Independence - Pressure at Wedge-Tip

As can be seen in *Figure **19*** and *Figure **20***, simulations are grid independent for discretisation above 40,000 cells. This suggests that the CFD model is reliable and results are valid. Further model validation can come from comparison with analytical and experimental results.

4.6 Results

Once the model was built and validated, results could be processed and investigated. *Figure **21*** and *Figure **22*** show the contours of pressure and temperature respectively.

Figure 21: Pressure Contour

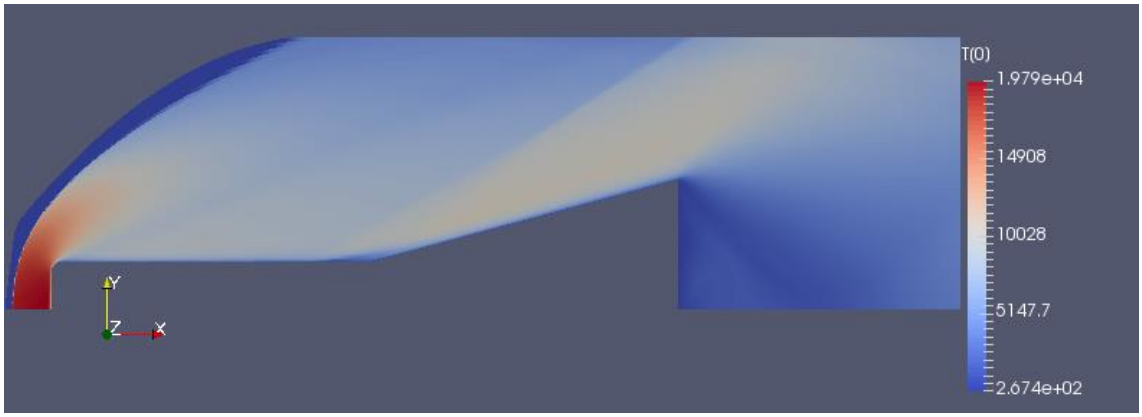

Figure 22: Temperature Contour

As can be seen, pressure and temperature peaks occur at the stagnation point. The peak pressure, once the flow simulation had settled, was approximately 37kPa. Equation 6 calculates the pressure ratio across a normal shock given perfect gas assumptions.

$$\frac{p_2}{p_1} = \frac{\left(2\gamma {M_1}^2 - (\gamma - 1)\right)}{\gamma + 1} \tag{6}$$

For the ratio of specific heats 'γ' = 1.4, free-stream Mach no. 'M_1' = 19.37, and free-stream pressure 'p_1' = 0.007978pa, the pressure behind the shock, 'p_2' was calculated to be 34.9 kPa. While bow-shocks cannot be treated as normal-shocks, there was an 'order-of-magnitude' agreement between the analytical and simulated post-shock pressures and this was used to justify early progress towards running higher fidelity simulations.

A bow shock stands off from the front of the nose and was measured to be 41.6mm (*Figure **23***).

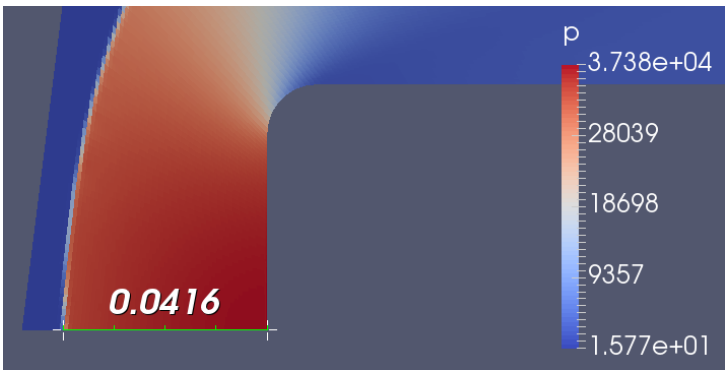

Figure 23: Bow Shock Stand-off

The simulation uses an ideal-gas model which underestimates the density resulting in an overestimation of the bow shock stand-off distance. Selection of, and investigation into, a more appropriate gas model is recommended as future research.

An oblique shock protrudes from the surface upstream of the wedge-tip. Two regions can be seen in *Figure **24***. A predominant oblique shock is apparent protruding from the tip, but a lighter region is seen upstream of the wedge-tip. This is also visible in the temperature profile and the effects of the boundary layer are more evident around the ROI (*Figure **25***).

Figure 24: Pressure at Wedge-Tip

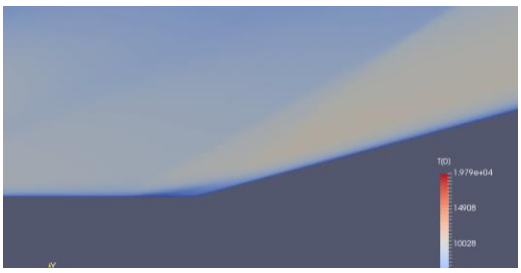

Figure 25: Temperature at Wedge-Tip

4.6.1 Oblique Shock Angle

Oblique shock theory was used to determine the angle of the oblique shock analytically. This was compared to angles measured in the simulation as an additional means of validation. Equation 7 relates the turning angle 'θ' to the oblique shock angle 'β', and the Mach number.

$$\tan\theta = \frac{2}{\tan\beta}\left[\frac{{M_1}^2 \sin^2\beta - 1}{{M_1}^2(\gamma - \cos 2\beta) + 2}\right] \tag{7}$$

Given that the Mach number and the turning angle are known, an iterative solver can be used to determine the angle of the oblique shock. *Figure **26*** presents the plot of local Mach number in the region of interest.

Figure 26: Mach number Probe

Mach numbers ranged from 2.4 – 2.8 in the region downstream of the bow shock and upstream of the oblique shock. Given the turning angle, 15°, the resulting analytical oblique shock angles were in the range of 38° – 34°. The location indicated in ***Figure 26*** returned a Mach number of 2.65 and an analytical oblique shock angle of 35.3°.

As can be seen in *Figure **25*** an oblique shock protrudes from the flat plate just upstream of the wedge-tip. *Figure **27*** and *Figure **28*** show the shock angles measured downstream and at the wedge-tip respectively.

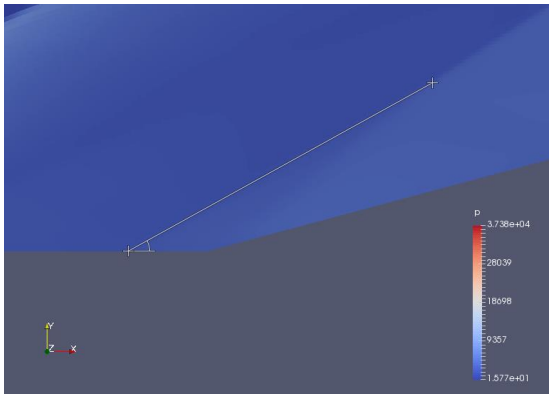

Figure 27: $\boldsymbol{\beta}$ = 29°

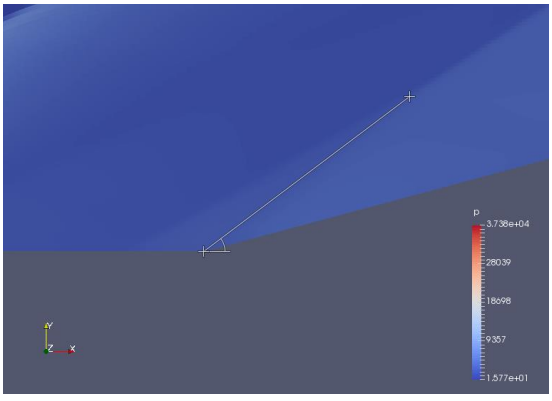

Figure 28: $\boldsymbol{\beta}$ = 37°

The analytically determined shock angle was 35.3° and this is in close agreement with *Figure **28*** (37°). Given that the equation does not account for boundary layer propagation along the flat plate this agreement is expected. The oblique shock angle in *Figure **27*** indicates that some interaction within the flow has led to the oblique shock beginning further upstream than expected and the contribution of boundary layer to this effect can be observed.

4.6.2 Boundary Layer Measurements

The distance of the upstream shift of the oblique shock is often approximated to be 4 times the thickness of the boundary layer. *Figure **29*** shows the measured stand-off distance and this can be compared with boundary layer thickness to investigate the validity of this approximation.

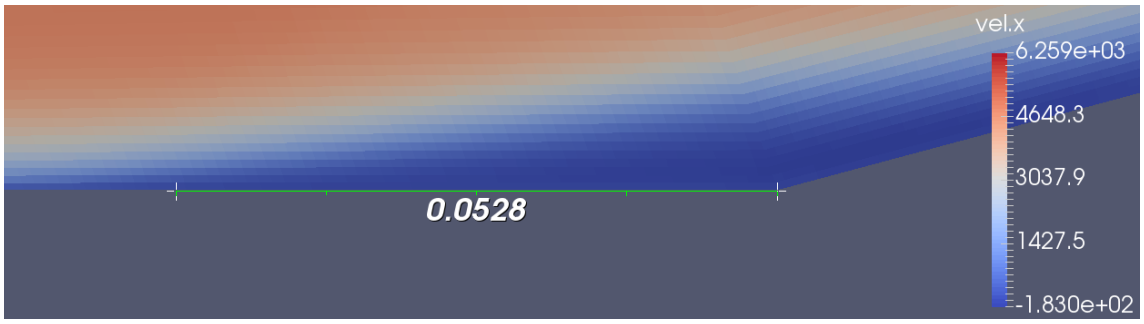

Figure 29: Shock Distance

The propagation of the boundary layer along the wall can be seen in the velocity profile. *Figure **30*** presents the plot of x-velocity along the discretised profile.

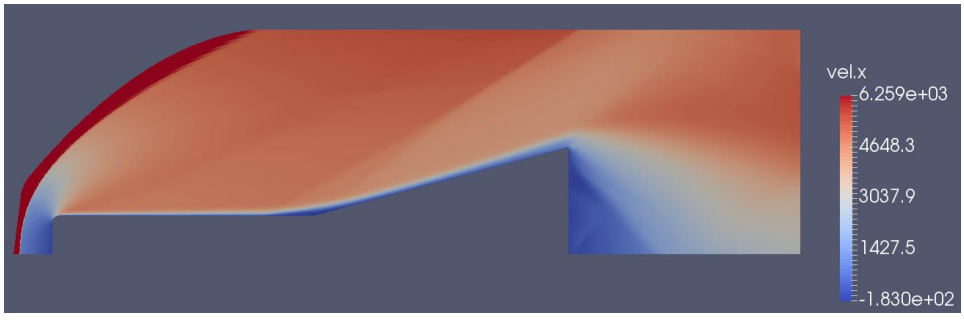

Figure 30: x-Velocity Profile

As expected, the velocity drops to zero at the nose. There are areas of negative velocity occurring in the wake close to the rear surface and this may be an interesting region to

investigate for future research. *Figure **31*** presents the x-velocity plot in the region of interest.

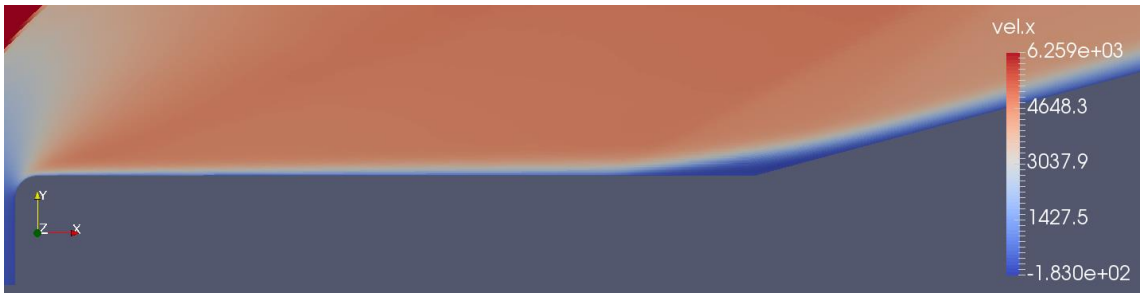

Figure 31: x-velocity Profile at the Wedge-Tip

The boundary layer can be seen to thicken along the surface. At the point measured in ***Figure 29*** there is a clear separation of the velocity profile and darker regions can be observed within the boundary layer further downstream. A thickness was measured on the velocity profile to be approximately 6.89mm (*Figure **32***).

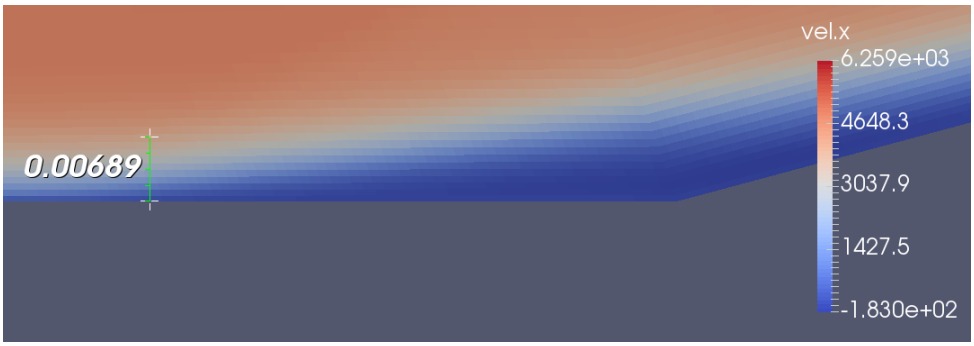

Figure 32: Boundary layer Thickness

The measured stand-off distance divided by the thickness is approximately 7.7 indicating that the current approximation (x4) is conservative in this case. A more rigorous investigation, into a range of flow fields and turning angles, could determine whether the approximation can be revised.

4.6.3 Boundary layer Interactions

Flow interactions within the boundary layer are of particular interest. Pressure, velocity, and density plots have been generated, first along the entire discretised surface of the profile. These are shown in *Figure **33***, *Figure **34***, and *Figure **35*** respectively.

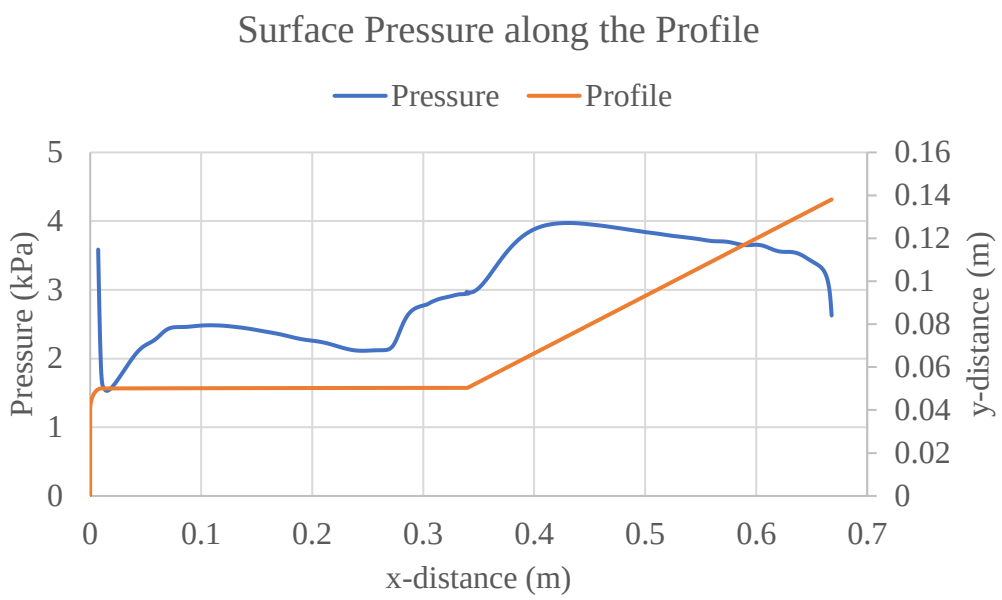

Figure 33: Surface Pressure along the Profile

*The pressure at the nose reaches 37kPa. Selected data was truncated to allow clearer observation along the rest of the surface profile.

Two increases in pressure are seen in the region of interest. The first begins at around 0.28m which is the observed stand-off distance, and then again at around 0.34m which is the wedge-tip. These jumps correlate to rapid decreases in velocity seen in *Figure **34***.

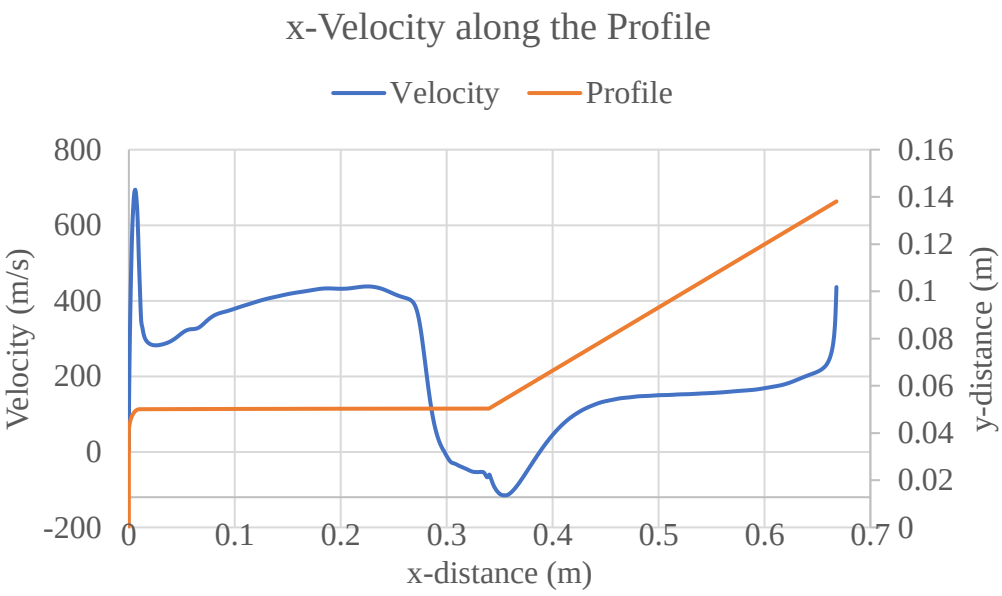

Figure 34: x-Velocity along the Profile

In addition to changes in velocity magnitude, the velocity profile drops below zero at around 0.3m and remains negative until around 0.39m. This indicates turbulence in the boundary layer in that region.

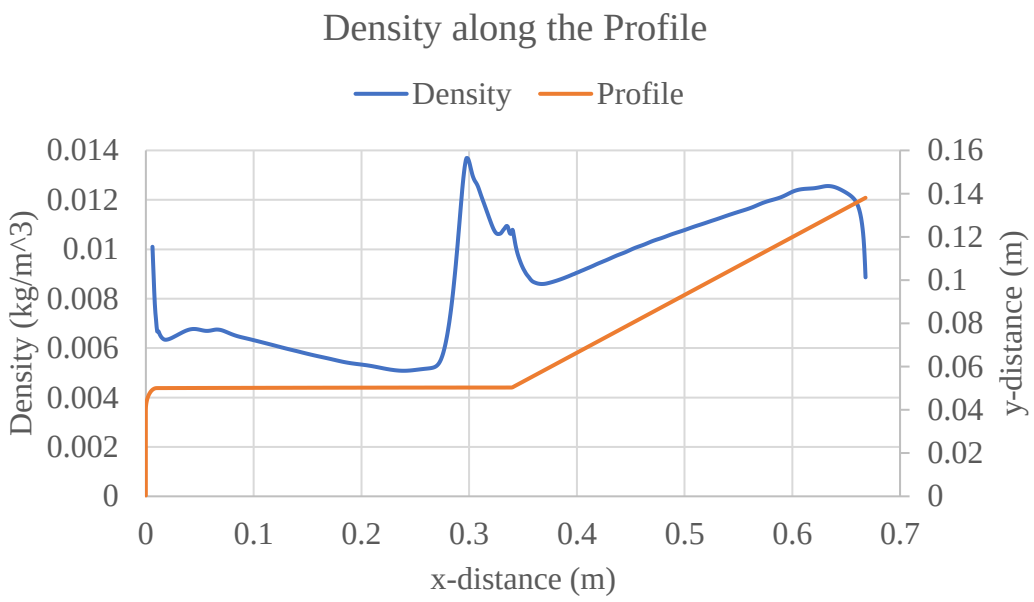

Figure 35: Density along the Profile

*The density at the nose reaches 0.064kg/m^3. Selected data was truncated to allow clearer observation along the rest of the surface profile.

A sharp change in properties is seen within the same region of all three plots. A rise in pressure and density occurs just as there is a sharp fall in velocity at around 0.28m. The influence of the wedge can also be seen in the three plots with another pressure rise, a small jump in density, and a decrease in velocity at 0.34m which is the tip of the wedge.

Further investigation of the boundary layer close to the wedge-tip was conducted. The previous three plots are of data along the surface. To investigate away from the surface a series of slices were taken using the 'slice-list' function within eimler3, given a specified i-range and j-range. Plots of pressure, velocity, and density vs. x-position were generated for a range of y-values. The plot x-range begins 0.26m from the nose and continues to the wedge-tip at 0.34m. Given the measured shock stand-off distance (*Figure **29***) the range for interesting results is between 0.28m and 0.34m.

*Figure **36***, *Figure **37***, and *Figure **38*** present plots of pressure, velocity, and density respectively.

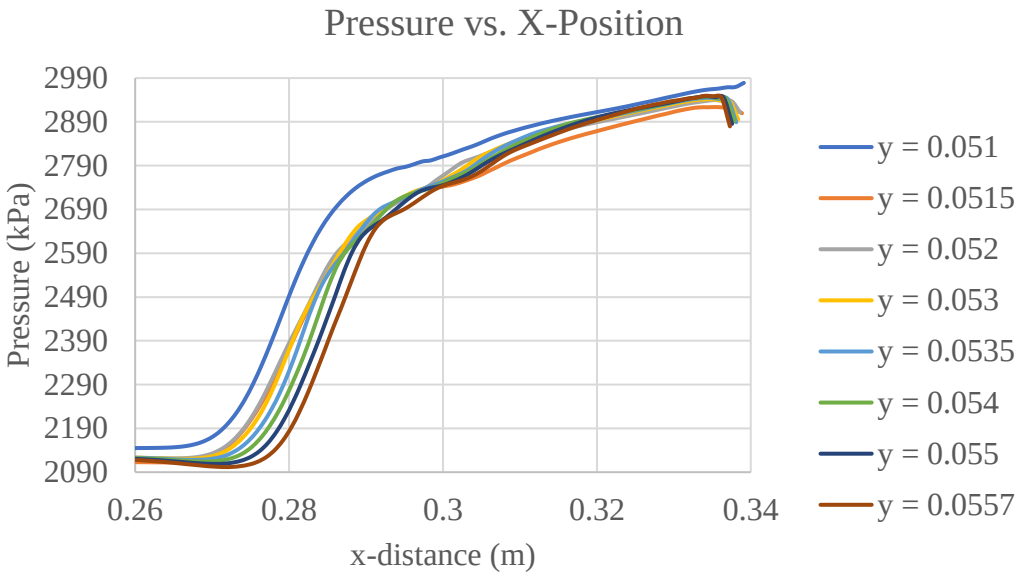

Figure 36: Pressure Profiles in the Boundary Layer

The model upper surface begins at y = 0.05m and each slice represents around a half millimetre step away from the model. The pressure profiles are closely bunched, and even overlap as they get closer to the wedge-tip at 0.34m.

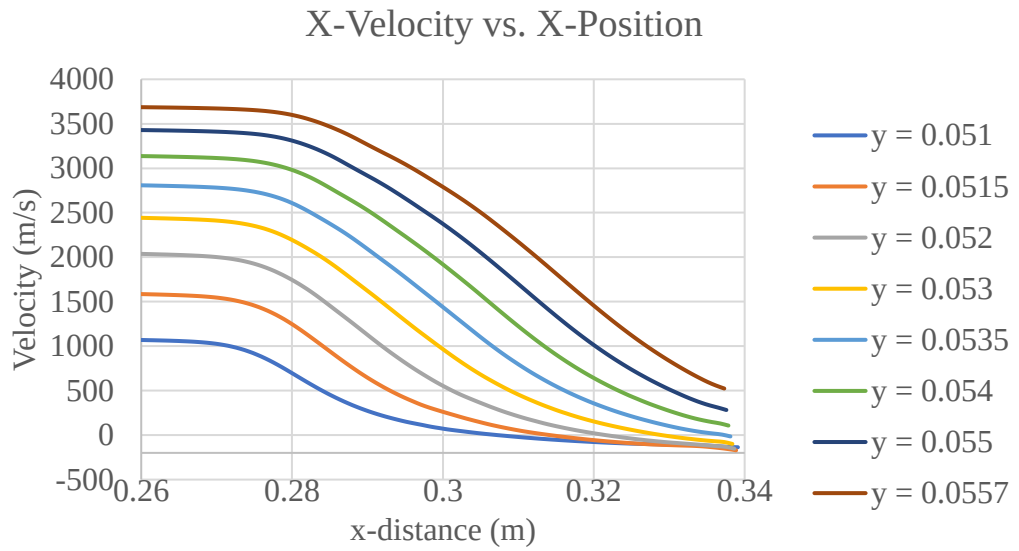

Figure 37: Velocity Profiles in the Boundary Layer

The velocity profiles seem more uniformly distributed and this aligns with the simple model of boundary layer growth. There are, however, regions where velocity profiles drop below zero, indicating a change in direction, and this occurs in the regions up to 3.5mm away from the surface.

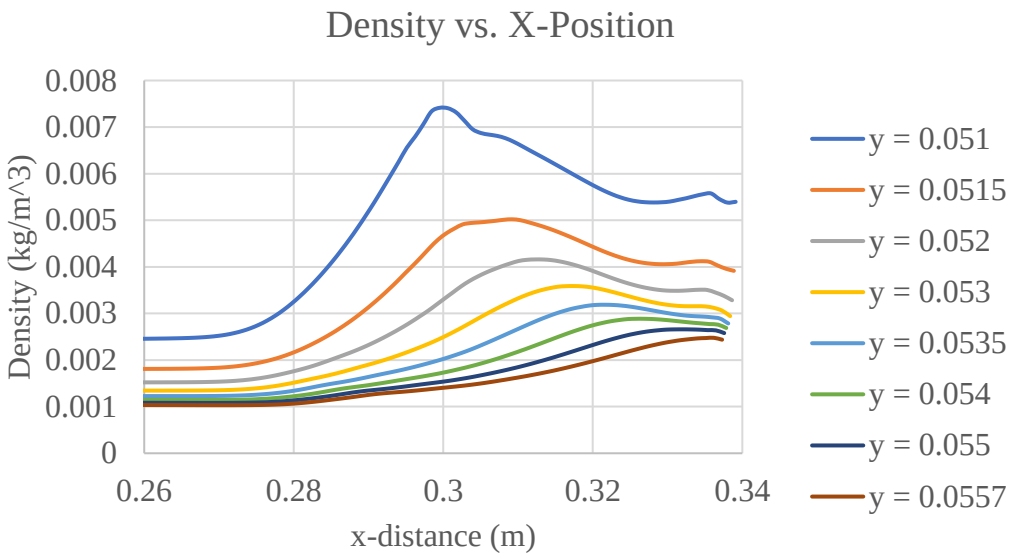

Figure 38: Density Profiles in the Boundary Layer

As can be seen in *Figure **38***, the density increases for each slice closer to the surface. This is expected within the boundary layer but of particular interest is the lateral movement of peaks for each increase in y-distance. Stepping away from the surface sees a density peak which shifts downstream, to the right. This is also indicative of a boundary layer and could be a means of measuring boundary layer displacement thickness.

4.7 Discussion

In the current models, clustering and meshing is designed to capture information at the wedge-tip. Minor modifications could be applied to focus on other areas of interest. The coarse meshes had artefacts in the flow around the outer edge of the bow shock. This was due to the shape of the block (block_2) and was exacerbated by any clustering towards the model surface. While increasing the cell count (in the y-direction) helped to remove artefacts appearing in the flow in that region, a restructured mesh would have been a more robust solution.

4.8 Summary

A 2D computational model was developed to simulate flow over QARMAN at the trajectory point. Blocking, meshing, and clustering was used to investigate the region of interest which was the interface of the fore-body and the wedge-tip. The effects of boundary layer propagation and displacement thickness were observed, and measurements were taken for comparison with analytically calculated dimensions. Measurements can also be taken on an experimental model and the design and construction of a scaled-model is discussed in Section 5.

The code used to run simulations in discussed in this chapter can be seen in Appendix A.

5. Scale Model Design

5.1 Introduction

This chapter discusses the design of a scaled-model of QARMAN. Section 5.2 discusses the assumptions and simplifications which influenced the model geometry. Section 5.3 discusses and justifies the chosen scaling factor. The designed model is presented in Section 5.4 and mounting considerations are discussed in Section 5.5. The assembled components are shown in Section 5.6 and the manufactured final product is presented in Section 5.7.

5.2 Model Simplifications

QARMAN is symmetric about its primary axis (in the line of trajectory) and the following simplifications were made to allow the model to be machined within time and cost constraints.

- Like the 2D CFD model, a scaled-model can be built with only the upper wedge included.
- The solar panels which deploy and act as a passive breaking system were modelled as a 15-degree wedge. The angle is the same as QARMAN however the hinge was not modelled.
- The nose geometry on QARMAN is not perfectly flat. A simplified flat surface with 2mm rounded edges was modelled as an approximation of the slightly more complex geometry.
- Materials should be easily sourced with regard to both type and size.

*Figure **39*** presents the profile of the actual nose shape beside the modelled nose shape.

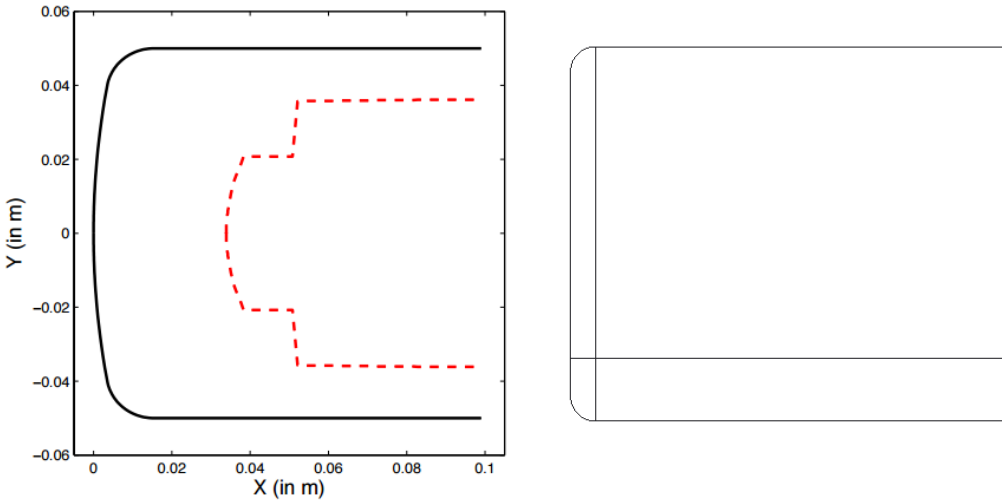

Figure 39: TPS vs. Modelled geometry [4]

QARMAN's geometry is slightly more complex than was modelled, and this would influence the shape of the bow-shock standing off from the front surface. The more complex geometry could have been built into the CFD model, however this shape for the scaled-model would be more complex, time consuming and expensive to machine. The modelled shape was a flat surface with a 2mm round on the four edges.

Because the wedges are separated by 90°, their interaction will be limited to the region very close to the corner, as indicated in *Figure **40***. A single wedge was modelled and it is thought that this will not affect the shock wave boundary layer interactions on the centreline greatly.

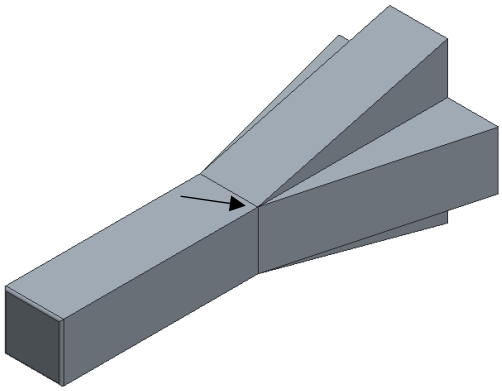

Figure 40: 3D Model of QARMAN

5.3 Model Scaling

The following factors formed the design parameters for the model scaling factor:

- The X2 nozzle exit is circular with a 208mm diameter (*Figure 7*). A core-flow diameter of 140mm is achievable [30] and this is the upper bound for the model.
- The model should be large enough to house instrumentation.
- The scaling factor should allow for accurate scaling of the model.
- The model should be simple enough to be made within time and cost constraints.

The diagonal dimension of a 1:1 scaled-model facing into the flow is 213mm. The maximum scale factor is therefore 140/213, – approximately ≈ 2:3.

Thin-film sensors have been considered for measuring heat transfer during experiments. The diameter of a thin-film sensor head is 2.5mm. Either 6 or 8 channel wiring harnesses were available for retrieving signal data from models. The model should be sufficiently large to house at least 8 thin-film sensors and their wiring.

The chosen scale factor should scale simply. The ratio should not return a repeating decimal as this can lead to needless complication with dimensioning. For this reason, while a 2:3 scale fits the above criteria, a 6:10 scale is more workable. A 6:10 scale means that a 100mm wide CubeSat scales to 60mm thickness materials. This was too large to source easily.

The chosen scale factor was 3:10 given the above considerations. The final design and mounting considerations are discussed further in subsequent sections.

5.4 Model Parts

Housing instrumentation, mounting the model, and assembling the parts were key design considerations. An upper and lower part allow for access to a hollowed recess so that instrumentation can be fitted easily within the model. For mounting, a wider recess was designed at the rear to mate with a mounting piece (*Figure **46***) and this is discussed further in Section 5.5. For assembly, all holes were countersunk to ensure bolt-heads did

not protrude from the model into the flow. *Figure **41*** and *Figure **42*** present the designed Upper, and Lower parts respectively.

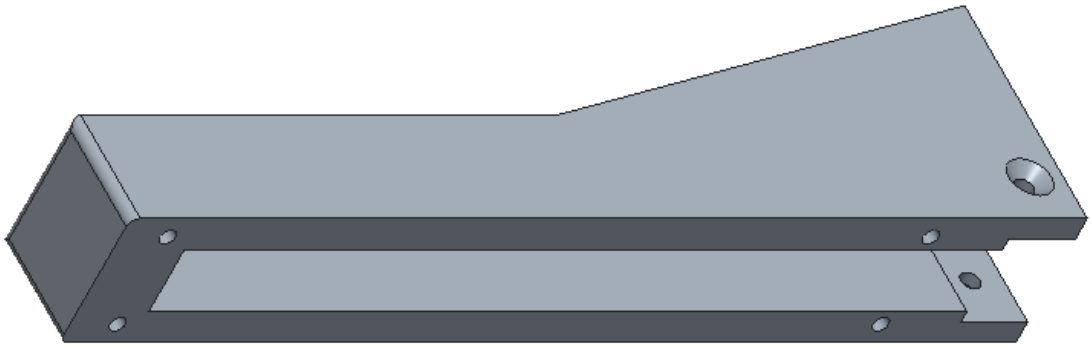

Figure 41: Upper Part

Figure 42: Lower Part

The holes were M4 threaded and countersunk holes. Their primary purpose is to hold the model parts together and to attach the model to the mount. The model and mounting parts were designed so that axial loads on the model are taken by the model body in compression and the fasteners should not experience critical shearing loads.

5.4.1 Thin-Film Positions

An available wiring scheme allowed for 8 sensors and the proposed experiment was designed to use that many. The thin-films have a head diameter of 2.5mm (after applying heat shrink tubing) and this was the required diameter for holes in the model. *Figure **43*** presents the top view of the upper part, which shows the location of holes along the upper surface of the model.

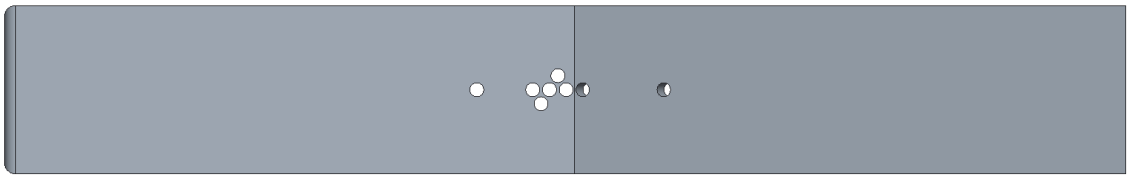

Figure 43: Thin-Film Hole Locations

One of the biggest uncertainties involves the boundary layer separation at the interface between fore-body and wedge. As can be seen, two holes are away from the centreline and this allows for a closer bunching of sensors near the wedge tip, to give better axial resolution. The clustered holes are spaced 1.5mm apart (in the x-direction) so that the five holes clustered to the left of the wedge-tip extend 8.75mm upstream. This space represents 29.17mm on the full 1:1 scale. From the CFD output, the region of interest is 52.8mm from the wedge-tip (*Figure **29***) and the spacing on the model was considered to be conservative enough to capture relevant data.

The offset holes are 1.5mm from the centreline (in the y-direction). The outer holes are 15mm further out and were placed as comparative data points to collect information outside the ROI. These positions were matched by history points in the CFD model. The bunching is designed to capture data about the specific region of interest at the wedge-tip. Further justification of the spacing, based on calculation of the boundary layer displacement thickness, is presented in Section 6.4.

5.5 Mounting Hardware Design

*Figure **44*** presents the Model Mounting System, which sits in the test section at the end of X2, and allows various options for mounting models (Source: personal correspondence with C. James, 2017).

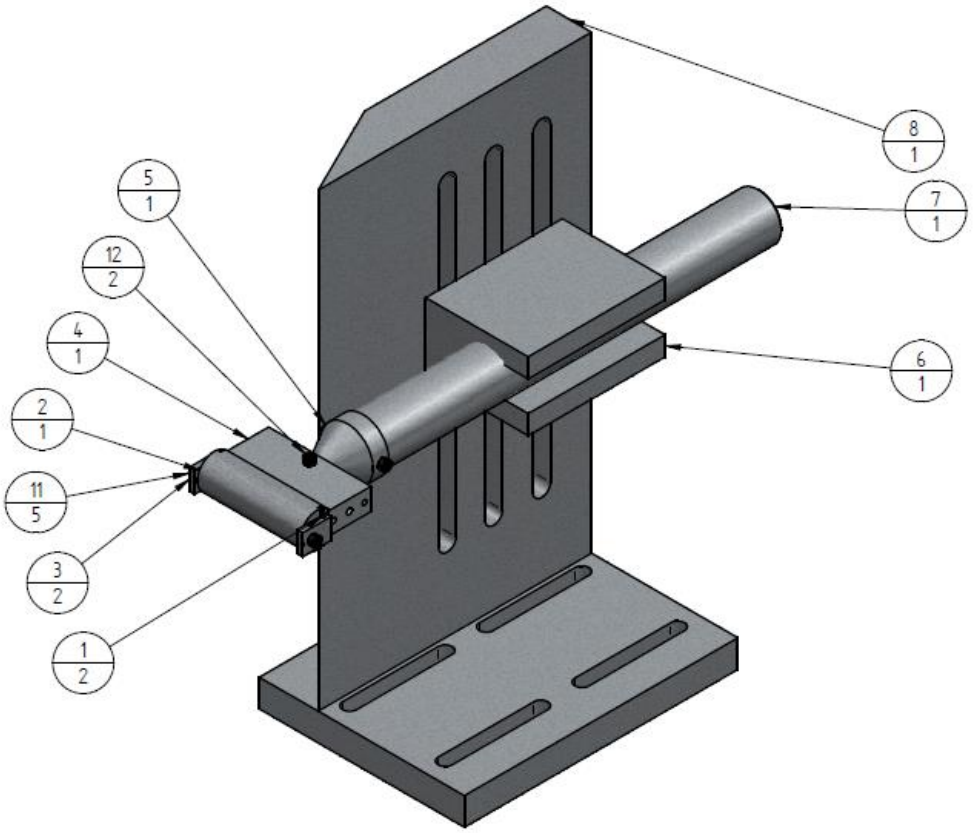

Figure 44: Model Mounting System

Two new parts were built to mount the scaled-model. A new sting (Part no. 7) was designed to be thicker to allow for deeper threading and additional strength (*Figure **45***). The outer diameter was machined to 33mm allowing for more precise fitting to attachments.

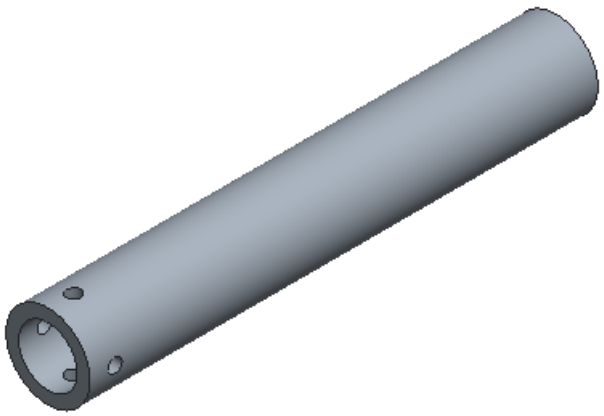

Figure 45: Sting

The mounting holes are M6 threaded holes. Their centre is 10mm from the front, compared to 5mm on the existing sting, and the added length will allow models or mounts to sit further down the sting providing more support. A new mount (Part no. 5) was designed with a squared front to restrict model rotation about the major axis (*Figure **46***).

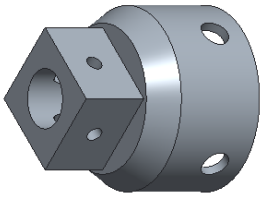

Figure 46: Square Mount

The holes in the rounded section are M6 unthreaded holes for mounting to the sting. The holes in the squared section are M4 threaded holes for mounting to the model. The model has a square recess, designed to sit flush against the flat front edge of the mount. This means that the axial loads, applied during experiments, are not taken as a shearing load on the bolts. Instead, like the model parts, the bulk of axial loading is taken in compression by the mounting pieces.

5.5.1 Buckling Analysis

The critical buckling load was determined for the sting using Euler column buckling theory. Equation 8 calculates the critical buckling load 'P_{cr}' given the Young's Modulus 'E', the area moment of inertia 'I', the effective length factor 'K', and the unsupported column length 'L'. The inner and outer radii of the sting were used to find the area moment of inertia using Equation 9.

$$P_{cr} = \frac{\pi^2 EI}{(KL)^2} \tag{8}$$

$$I = \frac{\pi}{2}({r_2}^4 - {r_1}^4) \tag{9}$$

The model was made with structural steel which has a Young's modulus of 200GPa. Table **5** presents the relevant properties and the resulting critical load.

Table 5: Buckling Properties

Young's Modulus	Effective length Factor	Unsupported Length	Outer Radius	Inner Radius	Area Moment of Inertia	Critical buckling Load
E	K	L	r_2	r_1	I	P_{cr}
200GPa	2	0.1m	0.0165m	0.0115m	8.895e-8	4.389MN

The mounting clamp is approximately 0.1m long and the remaining unsupported length of the sting was 0.1m. The effective length factor 'K' was chosen based on the fixed-free state off the sting since one end is supported in the mounting clamp and the other end is unsupported.

The existing sting has the same unsupported length, a 17mm outer radius, and a 15mm inner radius. The critical buckling load for this existing sting, which has a 2mm thickness, is approximately 2.55MN. By comparison, a new sting with only 1mm added thickness, – r_2 = 0.0165, r_1 = 0.0135 – would have a critical buckling load of 3.17MN.

5.6 Assembly

The model parts and mounting pieces were imported into an assembly. The assembly was investigated to ensure alignment of holes, edges, and corners. Any interference between edges was identified in early iterations as well as any hole-alignment issues. Once final refinements were made, the part files and drawings were sent to the workshop. *Figure **47*** presents an exploded view of the assembled components.

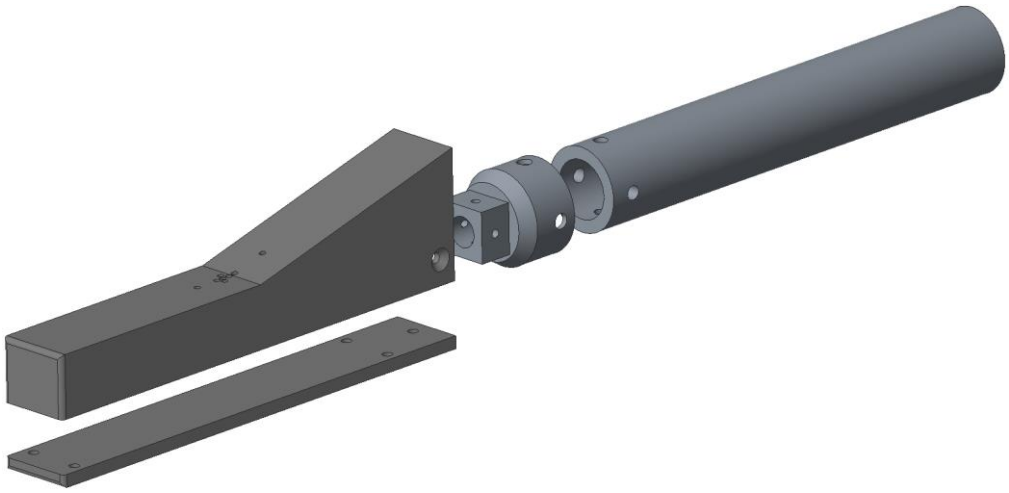

Figure 47: Assembly Exploded View

5.7 Manufactured Scale-Model and Mounting Hardware

The model and mounting pieces were machined by The University of Queensland's Mansergh Shaw workshop. *Figure **48*** to *Figure **53*** present the final machined parts and assemblies.

Figure 48: Upper CubeSat Section

Figure 49: Lower CubeSat Section

Figure 50: Assembled Model

Figure 51: Sting

Figure 52: Square Mount

Figure 53: Mounted Assembly

The removed material and space within the model did not have any specific tolerances, and needed only to be large enough to house instrumentation. The final mounted assembly was fastened with seven M4 bolts and four M6 bolts.

5.8 Summary

A 3:10 scaled-model of QARMAN was designed and built. The nose geometry was simplified and only the upper wedge of QARMAN was included. The position of eight thin-film sensors was outlined based on an investigation into boundary layer growth. These holes have not been machined but are recommended for conducting the experiment described in Section 6. All model and mounting parts were manufactured based on engineering drawings, and these can be seen in Appendix B.

6. Experiment Design

6.1 Introduction

This chapter details the design of experiments to be conducted in UQ's X2 expansion tube. Of interest for QARMAN is the heat transferred to the thermal protection system and the resulting ablation. QARMAN's profile, comprising the nose, fore-body, and wedge, provides an interesting geometry for experiments on other locations as well.

As discussed in previous chapters, the interface of fore-body and wedge, and the boundary layer separation across that region, is of particular interest for experiments. The propagation of a boundary layer was observed in the computational model and this can be compared with experiments.

The thickness of the boundary layer increases along the length of the model until it encounters the wedge. The wedge-tip, angled at 15 degrees from the horizontal, results in an oblique shock. Interaction between the boundary layer and the tip of the wedge means that the oblique shock begins upstream of the wedge-tip. The area beneath the oblique shock can experience interesting flow phenomena such as turbulence and boundary layer separation. This section forms the region of interest for experiments and further calculations have assisted in determining the correct domain.

Section 6.2 presents the method used to determine the post-shock density required for binary scaling. Section 6.3 presents results of an investigation of PITOT output and the resulting driver gas configurations which can produce a similar scaled post-shock density. Section 6.4 discusses calculation of a hypersonic boundary layer thickness and boundary layer displacement thickness. The analytical stand-off distance is compared with CFD output and this is discussed in Section 6.5 which outlines the proposed placement of sensors.

6.2 Post Shock Conditions

High free-stream temperatures occur in expansion tunnels. Between 5 and 10% of flow enthalpy can be stored as static enthalpy and, as a result, while the total enthalpy of the free-stream can be achieved, the flow Mach number will be lower than desired [30]. Test

conditions for scaled models will be different and determining scaled post-shock conditions is necessary.

The selected trajectory point occurs at 50km altitude, chosen as the point of peak-heating [4]. The Mach number and velocity at that point are 19.37 and 6350m/s respectively.

Table 6 presents the Mach number, velocity, and free-stream properties for the chosen trajectory point.

Table 6: Free-Stream Properties

Property	**Value**	**Nomenclature**
Mach no.	19.37	M
Velocity	6350m/s	v_∞
Altitude	50km	H
Temperature	270K	T_∞
Pressure	75.9pa	P_∞
Density	0.000977 kg/m^3	ρ_∞

A numerical solver, Chemical Equilibrium with Applications (CEA), developed by Gordon and McBride [31, 32], was used to find the post-shock binary product 'ρL' and Reynolds number. The characteristic length L for the full-scale vehicle is 0.1m and the scale model ratio is 3:10. Table **7** presents the CEA output relevant to post-shock scaling.

Table 7: Full-Scale and Scaled Post-Shock Density and Reynolds Number

	Full-Scale L = 0.1m	Scaled L = 0.03m
ρ kg/m^3	1.4563e-2	4.8543e-2
ρL kg/m^2	1.4563e-3	1.4563e-3
Re	32640.22	32640.22

6.3 PITOT Investigation

Scaled post-shock density was the design parameter for determining X2 fill conditions. X-Labs expansion tube code, PITOT, developed by James and colleagues [30, 33] was

used to determine the fill conditions required to replicate the flow in X2. Research conducted by Steven Lewis, from UQ's Centre for Hypersonics, provided PITOT output for a range of initial X2 fill conditions. The scaled post-shock density required to maintain ρL was found to be 0.04854kg/m^3 (Table **7**). Table **8** presents the fill conditions which produced densities closest to the required density.

Table 8: Potential Fill Conditions

Fill Condition	**P1** (pa)	**P5** (pa)	**Density** (kg/m^3)	**Margin** %	**Temperature** (K)
1.2mm He:0.8 Ar:0.2	2500	100	0.047298	2.626	6249.27
1.2mm He:0.9 Ar:0.1	3000	75	0.048458	0.169	6719.68
1.2mm He:1.0	1500	75	0.048738	0.404	7533.63

P1 and P5 represent the pressure-fills for the shock and acceleration tubes respectively. The density is the equilibrium flow density over the model. The fill condition most able to replicate the design-point density is a 90% Helium 10% Argon mix utilising a 1.2mm steel diaphragm. While all three fill conditions were able to reasonably reproduce the post-shock density, the 90% Helium 10% Argon mixture properties were investigated further in determining the boundary layer thickness.

The final fill condition chosen for experiments is shown in Table **9**.

Table 9: Experiment Fill Conditions

Experiment Fill Conditions			
Driver Gas	Primary Diaphragm	p1	p2
90%He, 10%Ar	1.2mm Steel	3kPa	75pa

6.4 Hypersonic Boundary Layer

During hypersonic flight, large velocity differences occur across boundary layers leading to a momentum deficit and high levels of shear stress and heat transfer in the boundary layer. An investigation into the boundary layer thickness was conducted by applying conservation of mass, momentum, and energy equations.

The fluid viscosity determines the flow properties for low Reynolds numbers. These flows are called laminar, where the flow is steady and smooth. For higher Reynolds numbers, the flow transitions to turbulent, the flow is unsteady, and solutions become increasingly difficult. To assess the validity of boundary layer measurements, it was necessary to determine whether the flow was laminar or turbulent. This was achieved by investigating the Reynolds number 'R_e' where:

$$R_{e,L} = \frac{\rho u_0 L}{\mu} \tag{10}$$

The density 'ρ' was taken from the PITOT investigation (Table **8**). The dynamic viscosity 'μ' was determined using the Sutherland Viscosity equation.

$$\mu = \mu_0 \left(\frac{T}{273}\right)^{3/2} \times \left(\frac{386}{T + 113}\right) \tag{11}$$

Where μ_0 is the reference viscosity at the reference temperature, taken to be 1.84E-5 (Pa.s). The temperature 'T' was taken from the PITOT investigation as the nozzle exit condition (Table **8**).

For a flat plate the transition from laminar to turbulent flow occurs when the Reynolds number is in the region of 300,000 to 500,000. The characteristic length 'L' is taken to be 0.102m; the distance from nose to wedge-tip on the scaled-model.

The resulting Reynolds number from Equation 10 is approximately 223,000 and the flow along the models' upper surface is therefore considered to be laminar.

The Boundary layer thickness, 'δ', and displacement thickness, 'δ^*' within hypersonic flows can be calculated using Equations 12 and 13 respectively.

$$\delta = \frac{x}{\sqrt{Re_x}} \left\{ 5 \frac{T_w}{T_\infty} + 0.68 \frac{\gamma - 1}{2} {M_\infty}^2 \right\} \tag{12}$$

$$\delta^* = \frac{x}{\sqrt{Re_x}} \left\{ 5 \frac{T_w}{T_\infty} + 0.68 \frac{\gamma - 1}{2} {M_\infty}^2 - 1.8 \right\} \tag{13}$$

Wall temperature, 'T_w', was approximated as room temperature, 298K. Flow Temperature, 'T_∞', was taken as 6719.68K (Table **8**). The Mach number was found to be 8.47 based on the sound speed and flow velocity exiting the nozzle.

Flow Mach number, as well as wall and flow temperatures, and the Reynolds number were then input into Equations 12 and 13 to determine boundary layer thickness and the displacement thickness. *Figure **54*** shows the calculated boundary layer propagation and displacement thickness along the horizontal surface behind the nose and up to the wedge-tip.

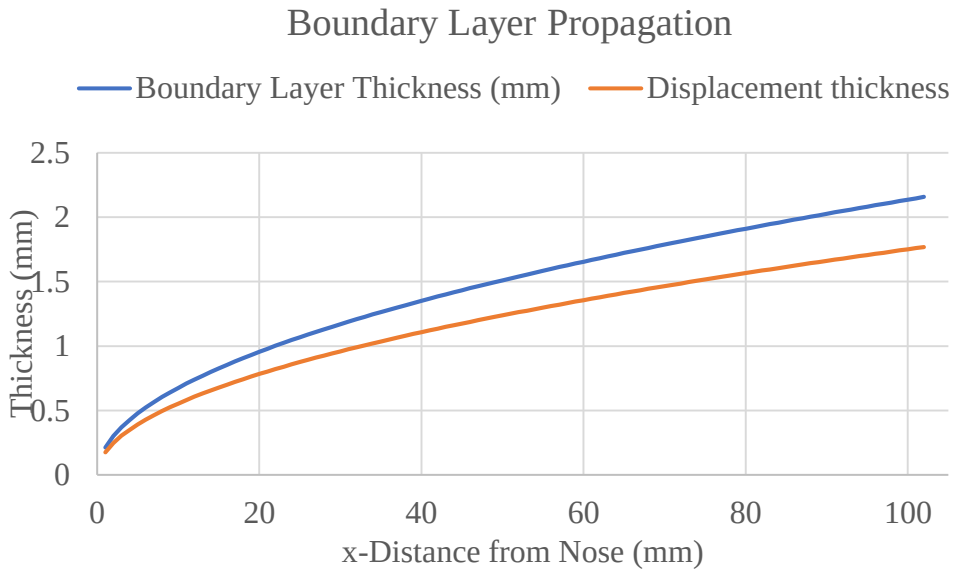

Figure 54: Boundary Layer and Boundary Layer Displacement Thickness

The predicted thicknesses at the wedge-tip (x = 0.102m) are presented in Table **10**.

Table 10: Boundary Layer Displacement Thickness

	Notation	Thickness (mm)
Boundary layer Thickness	δ	2.16
Boundary layer Displacement Thickness	δ^*	1.77

The displacement thickness was used as a design parameter for experiments.

As discussed in Section 4.6.2, shock stand-off is often approximated to be $4\times\delta^*$ times the displacement thickness. This represents a 7.07mm shift in the oblique shock, upstream of the wedge-tip. Measurements on the CFD output showed an even larger shift, approximately $7.7\times\delta^*$ (*Figure **29*** and *Figure **32***). This represents a 13.55mm shift upstream of the oblique shock. Disagreement between the analytical the computational model can be investigated through experiments, and the placement of sensors within the model is therefore important.

6.5 Sensor Placement

The number of sensors was dictated first by the available space within the model. An existing wiring setup has 8 spaces for sensors and this was considered to be sufficient for capturing data within the region of interest. The model could potentially house wiring for 12 sensors which could be utilised for future experiments.

As discussed in Section 4.1 the 3D flow effects propagate towards the centreline from the edge. As discussed in Section 5.2, on a full 3D model the wedges are separated by 90° and their interaction will be limited to the region very close to the corner (*Figure **40***). For these reasons, the sensors were bunched as close to the centreline as possible, while remaining within both analytical and CFD predicted shock stand-off regions.

Six thin-film gauges were bunched near the wedge-tip; five on the horizontal surface, and one on the wedge. The remaining two were placed outside the ROI as comparative data points for the experiment. *Figure **56*** presents the chosen thin-film locations as well as the shock stand-off distances predicted by CFD and analytical calculations. For reference, the velocity profile from CFD output is presented in *Figure **55***.

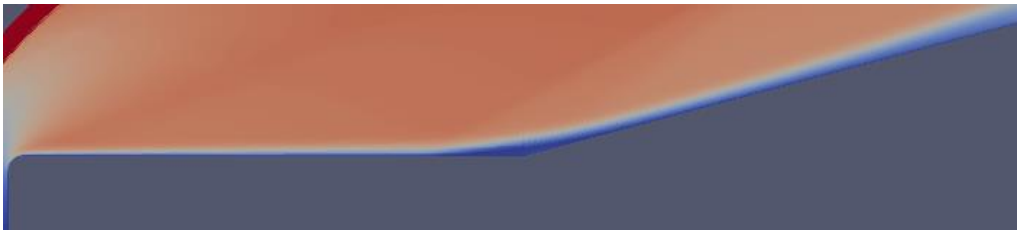

Figure 55: CFD Velocity Profile

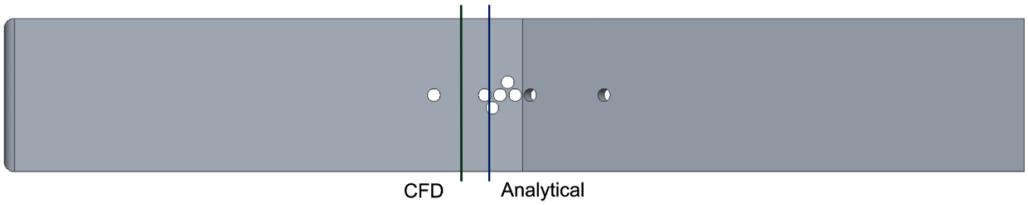

Figure 56: Thin Film Holes and Predicted Shock Stand-off Locations

As can be seen, four holes are clustered within both regions, and one is outside the analytically predicted region and within the CFD predicted region.

6.6 Summary

An experiment was designed to investigate boundary layer propagation and the resulting oblique shock stand-off, at the interface of fore-body and wedge-tip. Scaled, post-shock conditions were determined using the numerical tool CEA, and the resulting post-shock density was evaluated using a binary scaling technique. Investigation of PITOT output returned three potential driver gas configurations and the most accurate configuration was investigated further. A hypersonic boundary layer thickness was calculated and this informed the placement of sensors for the experiment. Comparison with CFD output determined that the analytical approach may underestimate the shock stand-off distance (or vice versa). This forms the motivation for the proposed experiment.

7. Conclusions & Recommendations

7.1 Conclusions

Goal 1 was to build a trajectory model able to determine the velocity of QARMAN upon re-entry. A velocity range of 7.5km/s < V_e < 7.67km/s was found and, in conjunction with the expected altitude of peak heating, was used to define conditions for the CFD model and the design of experiments.

Goal 2 was to develop a computational model able to simulate flow conditions over QARMAN at the selected trajectory point. The trajectory point was 50km altitude and the atmospheric conditions at that altitude, along with the velocity were used to simulate the flow conditions using UQ's in-house compressible flow code eilmer3.

The CFD model was validated through a study of grid-independence, as well as comparison with the analytically calculated oblique shock angle. Additional validation can come from comparison with experimental results and this is recommended for further research.

Goal 3 was to build a scaled-model of QARMAN. A 3:10 scale was chosen as it simplified calculations while still making use of the available core flow. In addition to the two model parts, two additional mounting parts were built in UQ's Mansergh Shaw workshop. A new sting with added thickness, and a square mounting piece, were manufactured, and these parts can be used for future projects in X2.

Goal 4 was to design an experiment. The chosen trajectory point was that of peak heating. The numerical solver, CEA, was used to determine the binary product 'ρL' for the trajectory point. After applying the scaling factor, ρL was maintained to determine the scaled post-shock density. PITOT output, provided by S. Lewis from UQ's Centre for Hypersonics, was consulted to determine an appropriate X2 driver configuration.

An investigation into hypersonic boundary layer propagation informed the placement of sensors upstream of the wedge-tip. The region is of interest because boundary layer displacement thickness influences the position of the oblique shock and this is an area of hypersonics warranting further exploration.

7.2 Recommendations

Further scope can come from placing sensors at the nose to capture heat data on the stagnation point. This data can inform the development of TPS and, in conjunction with a validated CFD model, presents an inexpensive means of predicting heat transfer and other flow phenomena.

There were artefacts within the coarse meshes of the CFD simulation. These were addressed by increasing the cell count but it is recommended that the blocking layout be restructured so that clustering does not exacerbate skew issues and so that results from future simulations are more robust to changes in the region of interest.

3D flow effects should not be ignored. Given the Mach number down-stream of the bow shock, perturbations from flow effects at the edges will reach the centreline before encountering the wedge at 340mm. This means that there will be a discrepancy between the CFD model and real-world results. Given that there are two planes of symmetry, a 3D model could be build which captures one quadrant of that symmetry and could appropriately simulate the 3D flow effects.

All simulations focussed on a zero angle of attack. It is reasonably simple to change the Angle of Attack (AoA). Further investigation into an AoA regime would provide interesting results. Shock shape, boundary layer displacement thickness, and a changing temperature profile could all be investigated by making small alterations to the code.

The nose of QARMAN has additional complexity which was not replicated on the model. The shape of the Bow shock would be slightly different and this can have implications for heat transfer and other flow phenomena. A simple approach would be to modify the CFD structure to better capture the nose shape. The additional curvature could also be replicated on the model for experimentation and this would be useful for comparison with re-entry data from QARMAN in the future.

References

[1] National Aeronautics and Space Administration (NASA). (2015). *CubeSat data analysis revision*. [Online]. Available: https://sma.nasa.gov/docs/default-source/News-Documents/cubesat-data-analysis.pdf?sfvrsn=0

[2] QB50. (2017). *What is a cubesat?* [Online]. Available: https://www.qb50.eu/index.php/project-description-obj

[3] Bailet, G., Bourgoing, A., Magin, T. and Laux, C. H., "Radiative and ablative studies for in-flight validation on reentry platforms." *International Planetary Probe Workshop*, Cologne, Germany, 15-19 June 2015.

[4] Bailet, G., Sakraker, I., Scholz, T. and Muylaert, J., "Qubesat for Aerothermodynamic research and measurement on abalation." *4th International ARA Days*, Archaon, France, 27-29 May 2013.

[5] Fahy, E. J., Gollan, R. J., Buttsworth, D. R., Jacobs, P. A., and Morgan, R. G., "Expansion tube and computational fluid dynamics studies of superorbital Earth re-entry." *46th AIAA Thermophysics Conference*, Washington, D.C., USA, 13-17 June 2016.

[6] Lewis, S. W., Morgan, R. G., McIntyre, T. J., Alba, C. R. and Greendyke, R. B. "Expansion tunnel experiments of Earth reentry flow with surface ablation," *Journal of Spacecraft and Rockets*, Vol. 53, No. 5, 2016, pp. 887-899.

[7] Jacobs, C. M., McIntyre, T. J., Morgan, R. G., Brandis, A. M.and Laux, C. O., "Radiative heat transfer measurements in low-density titan atmospheres," *Journal of Thermophysics and Heat Transfer*, Vol.29, No.4, 2015, pp. 835-44.

[8] Hicks, K. D., *Introduction to astrodynamics re-entry*, Military Bookshop Co: UK, 2009.

[9] Hohmann, W. (1960). *The attainability of heavenly bodies, NASA Technical Translation.* [Online] Available: https://ia800502.us.archive.org/12/items/nasa_techdoc_19980230631/19980230631.pdf

[10] Temam, R., *Navier-stokes equations theory and numerical analysis*. AMS Chelsea Publishing: New York, 1984.

[11] Sockacki, J. (2016). *Introduction to compressible computational fluid dynamics*. [Online] Available: http://educ.jmu.edu/~sochacjs/navierstokes.pdf

[12] Jacobs, P. A., Gollan, R. J., Jahn, I., and Potter. D. P. *The eilmer3 code: User guide and example book 2015 edition. Mechanical Engineering Report 2015/07*. School of Mechanical & Mining Engineering, The University of Queensland: Brisbane, 2015.

[13] Stalker, R. J., "Isentropic compression of shock tube driver gas," *ARS JOURNAL*, Vol. 30, No. 6, 1960, pp. 564-564.

[14] Stalker, R. J. and Morgan, R. G., "The University of Queensland free piston shock tunnel T4: initial operation and preliminary calibration." *4th National Space Engineering Symposium, IEAust,* Adelaide, Australia, 12-14 July 1988.

[15] Centre for Hypersonics, University of Queensland. (2016). *T4 - Free-piston driven shock tunnel*. [Online]. Available: http://hypersonics.mechmining.uq.edu.au/t4

[16] Resler, E. L., and Bloxsom, D. E., *Very High Mach Number Flows by Unsteady Flow Principles*, Cornell University Graduate School of Aeronautical Engineering, Limited Distribution Monograph: Ithca, 1952.

[17] Miller, C. G., and Jones, J. J., "Development and performance of the NASA Langley Research Center expansion tube/tunnel, a hypersonic-hypervelocity real-gas facility." *Proceedings of the 14th International Symposium on Shock Waves*, University of New South Wales Press, Sydney, Australia, August, 1983.

[18] Paull, A., Stalker, R. J., "Scramjet testing in the T3 and T4 hypersonic impulse facilities," in *Scramjet Propulsion, Progress in Astronautics and Aeronautics*, E. T. Curran and S. N. Murthy, Eds. Reston, Virginia: AIAA, 2000, pp. 1–46.

[19] James, C. M., Gildfind, D. G., Lewis, S.W., and Morgan, R. G., "Simulating and quantifying expansion tube flow conditions using compressible and isentropic flow relations," to be published.

[20] Gildfind, D. E., Morgan, R. G., and Jacobs, P. A., "Expansion in Australia," in *Experimental methods of shock wave research*, O. Igra and F, Seiler, Eds. Switzerland: Springer International Publishing, 2016.

[21] Buiter, T., "Improvement designs for the diaphragm systems on the University of Queensland's shock tunnels X2 & X3" Honours thesis, University of Queensland, St Lucia, Australia, 2007.

[22] de Crombrugghe, G., Gildfind, D., Zander, F., McIntyre, T., and Morgan, R., "Design of Test Flows to Investigate Binary Scaling in High Enthalpy CO2−N2 Mixtures" *19th Australasian Fluid Mechanics Conference*, Melbourne, Australia, 8-11 November 2014.

[23] Morgan, R. G, "Modelling of radiating flows in the atmospheres of the gas giants." 17th *Australasian Fluid Mechanics Conference*, Auckland, New Zealand, 5-9 December 2010.

[24] Martin, L. C., and Holanda, R., "Applications of thin film thermocouples for surface temperature measurement." *Spin-off technologies for commercial sensors and scientific instrumentation*, San Diego, California, 24-29 July 1994.

[25] Boutier, A., *New trends in instrumentation for hypersonic research*, Nato Science Series E: Châtillon, France, 1992.

[26] Schultz, D. L., and Jones, T. V., *Heat transfer measurements in short duration hypersonic facilities*, NATO Advanced Group for Aerospace Research and Development: Paris France, 1973.

[27] Oldfield, M. L., Jones, T.V and Schulz, D. L., "On-line computer for transient turbine cascade instrumentation," *IEEE Transactions on Aerospace and Electronic Systems*, Vol. AES-14, No. 5, 1978, pp. 738-749.

[28] Griebel, H., *Reaching high altitudes on Mars with an inflatable hypersonic drag ballon (Ballute)*, Deutsche Nationalbibliothek: Munich, Germany, 2010.

[29] Makky, A. A. (2016). *Computational fluid dynamics is the future*. [Online]. Available: http://cfd2012.com/cfl-condition.html

[30] James, C., Gildfind, D., Morgan, R., Lewis, S., Fahy, E., and McIntyre, T., "On the Current Limits of Simulating Gas Giant Entry Flows in an Expansion Tube," *20th AIAA International Space Planes and Hypersonic Systems and Technologies Conference*, Glasgow, Scotland, July 6-9, 2015.

[31] Gordon, G. and McBride, B., *Computer Program for Calculation of Complex Chemical Equilibrium Compositions and Applications I. Analysis*, NASA Lewis Research Center, Cleveland, OH, U.S.A., 1994.

[32] McBride, B. and Gordon, G., *Computer Program for Calculation of Complex Chemical Equilibrium Compositions and Applications II*. Users Manual and Program Description, NASA Lewis Research Center, Cleveland, OH, U.S.A., 1996.

[33] James, C., Gildfind, D., Morgan, R., Jacobs, P., and Zander, F., "Designing and Simulating High Enthalpy Expansion Tube Conditions," *2013 Asia-Pacific International Symposium on Aerospace Technology*, Takamatsu, Japan, 2013.

Appendix

A. CFD Code

```
#file cubesat.py
#Author Steve Apirana
#Developed in consultation with eilmer3 user guide and existing scripts
import numpy as np
theta = np.deg2rad(15)
#____Set individual global data attributes.
gdata.dimensions = 2
gdata.title = "Mach 19.37 flow over cubesat."
gdata.axisymmetric_flag = 0
#____Accept defaults for air (R=287 J/kg.K, gamma=1.4)
select_gas_model(model='ideal gas', species=['air'])
#____Initial simulation conditions
M_inf = 19.37
p_inf = 0.007978e4   #Pa
T_inf = 270.    #K
T_wall = T_inf # degree K --assumed cold-wall temperature
height = (0.05 + (0.34*np.sin(theta)))*1.2
#____Dummy used to pull sound speed
dummy = FlowCondition(p=p_inf, T=T_inf)
a_inf = dummy.flow.gas.a
u_inf = M_inf*a_inf
initial = FlowCondition(p=p_inf/3., T=T_inf, u=0., v=0.)
inflow  = FlowCondition(p=p_inf, T=T_inf, u=u_inf, v=0.)
#----------------------Nodes-------------------------------------------------

r = 0.01

a = Node(0.0,0.0, label="a")
b = Node(0.0,0.05 - r, label="b")
c = Node(0.0 + r,0.05, label="c")
d = Node(0.34,0.05, label="d")
e = Node(d.x + (.34*np.cos(theta)) ,d.y + (.34*np.sin(theta)),
label="e")
f = Node(e.x + 0.3, e.y + 0.04, label="f")

a1 = Node(a.x - 0.05, a.y, label="a1")
b1 = Node(b.x - 0.05 + 0.01, c.y + 0.03, label="b1")
c1 = Node(b.x - 0.03, c.y + 0.1 - 0.05, label="c1")
d1 = Node(d.x - (abs(d.x-c.x))*(1./4.), b.y + 0.25, label="d1")
e1 = Node(e.x, d1.y, label="e1")
f1 = Node(f.x, e1.y, label="f1")

e0 = Node(e.x, a.y, label="e0")
f0 = Node(f.x, a.y, label="f0")

bz = Node((b.x - (abs(b1.x-b.x))*(2./4.)),(b.y + (abs(b1.y-
b.y))*(2./4.)), label="bz")
cz = Node((c.x - (abs(c1.x-c.x))*(2./4.)),(c.y + (abs(c1.y-
c.y))*(2./4.)), label="cz")

#____Ghost Nodes
gx = r - r*np.cos(np.deg2rad(45))
gy = r - r*np.sin(np.deg2rad(45))
```

```
g = Node(c.x, b.y, label="g")
g1 = Node(c1.x, b1.y, label="g1")

#____Bezier Nodes along the boundary

#____Block 1 NORTH
Bz1 = Node((b1.x + (abs(b1.x-c1.x))*(0.45)),(b1.y + (abs(b1.y-
c1.y))*0.70), label="Bz1")

#____Block 2 NORTH
Bz2 = Node((c1.x + (abs(c1.x-d1.x))*(0.5)),(c1.y + (abs(c1.y-
d1.y))*0.9), label="Bz2")
Bz3 = Node((e.x + (abs(e.x-f.x))*(0.4)),f.y, label="Bz3")

#----------------------Lines----------------------------------------------

#____CubeSat Edge
ab = Line(a,b)
bc = Arc(b,c,g)
cd = Line(c,d)
de = Line(d,e)

#____Boundary Edge
a1b1 = Line(a1,b1)
b1c1 = Bezier([b1,Bz1,c1])
c1d1 = Bezier([c1,Bz2,d1])
d1e1 = Line(d1,e1)

#____Radiating lines
aa1 = Line(a,a1)
bb1 = Bezier([b,bz,b1])
cc1 = Bezier([c,cz,c1])
dd1 = Line(d,d1)
ee1 = Line(e,e1)

#____Trailing Blocks

ef = Bezier([e,Bz3,f])
e0f0 = Line(e0,f0)
e1f1 = Line(e1,f1)
e0e = Line(e0,e)
f0f = Line(f0,f)
ff1 = Line(f,f1)

#----------------------Clustering-----------------------------------------

cf1 = RobertsClusterFunction(1,0,1.09)
cf2 = RobertsClusterFunction(0,1,1.09)
#cf1 = None
#cf2 = None

#____Mesh 10------120400 cells

ny = 100
nx0 = 50        #Block 0
nx1 = 14        #Block 1
nx2 = 300       #Block 2
nx3 = 360       #Block 3
nx4 = 240       #Block 4
nx5 = 240       #Block 5
```

```
#----------------Blocking----------------------------------------
blk_0 = Block2D(make_patch(a1b1, bb1, ab, aa1), nni=nx0, nnj=ny,
              fill_condition=initial,
              cf_list = [None, cf1, None, cf1] ,label="BLOCK-0",
              xforce_list=[0,0,1,0])

blk_1 = Block2D(make_patch(b1c1, cc1, bc, bb1), nni=nx1, nnj=ny,
              fill_condition=initial,
              cf_list = [None, cf1, None, cf1] ,label="BLOCK-1",
              xforce_list=[0,0,1,0])

blk_2 = Block2D(make_patch(c1d1, dd1, cd, cc1), nni=nx2, nnj=ny,
              fill_condition=initial,
              cf_list = [None, cf1, None, cf1] ,label="BLOCK-2",
              xforce_list=[0,0,1,0])

blk_3 = Block2D(make_patch(d1e1, ee1, de, dd1), nni=nx3, nnj=ny,
              fill_condition=initial,
              cf_list = [None, cf1, None, cf1] ,label="BLOCK-3",
              xforce_list=[0,0,1,0])

blk_4 = Block2D(make_patch(e1f1, ff1, ef, ee1), nni=nx4, nnj=ny,
              fill_condition=initial,
              cf_list = [None, cf1, None, cf1] ,label="BLOCK-4",
              xforce_list=[0,0,0,0])

blk_5 = Block2D(make_patch(ef, f0f, e0f0, e0e), nni=nx5, nnj=ny,
              fill_condition=initial,
              cf_list = [None, cf2, None, cf2] ,label="BLOCK-5",
              xforce_list=[0,0,0,0])
```

```
#____Boundary conditions
identify_block_connections()
blk_0.bc_list[NORTH] = SupInBC(inflow, label="inflow-
boundary")
blk_1.bc_list[NORTH] = SupInBC(inflow, label="inflow-
boundary")
blk_2.bc_list[NORTH] = SupInBC(inflow, label="inflow-
boundary")
blk_3.bc_list[NORTH] = SupInBC(inflow, label="inflow-
boundary")
blk_4.bc_list[NORTH] = SupInBC(inflow, label="inflow-
boundary")

blk_0.bc_list[SOUTH] = FixedTBC(T_wall, label="Fixed T")
blk_1.bc_list[SOUTH] = FixedTBC(T_wall, label="Fixed T")
blk_2.bc_list[SOUTH] = FixedTBC(T_wall, label="Fixed T")
blk_3.bc_list[SOUTH] = FixedTBC(T_wall, label="Fixed T")

blk_5.bc_list[WEST] = FixedTBC(T_wall, label="Fixed T")

blk_4.bc_list[EAST] = ExtrapolateOutBC(label="outflow-
boundary")
blk_5.bc_list[EAST] = ExtrapolateOutBC(label="outflow-
boundary")
blk_5.bc_list[SOUTH] = ExtrapolateOutBC(label="outflow-
boundary")
```

```
#----------------global data settings----------------------------------------

gdata.viscous_flag = 1
gdata.flux_calc = ADAPTIVE
gdata.gasdynamic_update_scheme = "classic-rk3"
gdata.cfl = 0.9
gdata.dt = 1.0e-8
flow_time = height/u_inf
gdata.max_time = 15.*flow_time  # seconds
gdata.max_step = 230000
gdata.dt_plot = gdata.max_time/50.
gdata.dt_history = 1.0e-6

sketch.xaxis(-0.2, 0.8, 0.2, -0.05)
sketch.yaxis(0.0, 1.5, 0.2, -0.05)
sketch.window(-0.1, -0.2, 1., 0.5, 0.05, 0.05, 0.17, 0.17)
```

```
#----------------Processing Commands-----------------------------------
"""
e3prep.py --job=cubesat_2 --do-svg                          #prep
e3post.py --job=cubesat_2 --vtk-xml --tindx=all --add-mach     #post
e3shared.exe --job=cubesat_2 --run                          #solves (less
efficient)
#____miprun uses more cores to solve blocks
mpirun -np 6 e3mpi.exe -f cubesat_2 --run                   #solves 6
blocks
paraview plot/cubesat_2.pvd                                 #open paraview

e3post.py --job=cubesat_2 --vtk-xml --tindx=last --add-mach --slice-
list="0,:,0,0;1,:,0,0;2,:,0,0;3,:,0,0"

#____post processing for grid independence output
e3post.py --job=cubesat_2 --output-file=pressure.data --vtk-xml --
tindx=last --add-mach --slice-list="0,0,0,0;3,0,0,0"

#____post processing for 'P', 'v', 'rho' along the surface
e3post.py --job=cubesat_2 --output-file=pressure.data --vtk-xml --
tindx=last --add-mach --slice-list="0,:,0,0;1,:,0,0;2,:,0,0;3,:,0,0"

#____post processing for boundary layer (fore-body)
e3post.py --job=cubesat_2 --output-file=boundarylayer.data --vtk-
xml --tindx=last --add-mach --slice-list="2,225:300,1:25,0"

#____post processing for boundary layer (wedge)
e3post.py --job=cubesat_2 --output-file=boundarylayerwedge.data --
vtk-xml --tindx=last --add-mach --slice-list="3,1:75,1:25,0"
"
```

B. Engineering Design Drawings

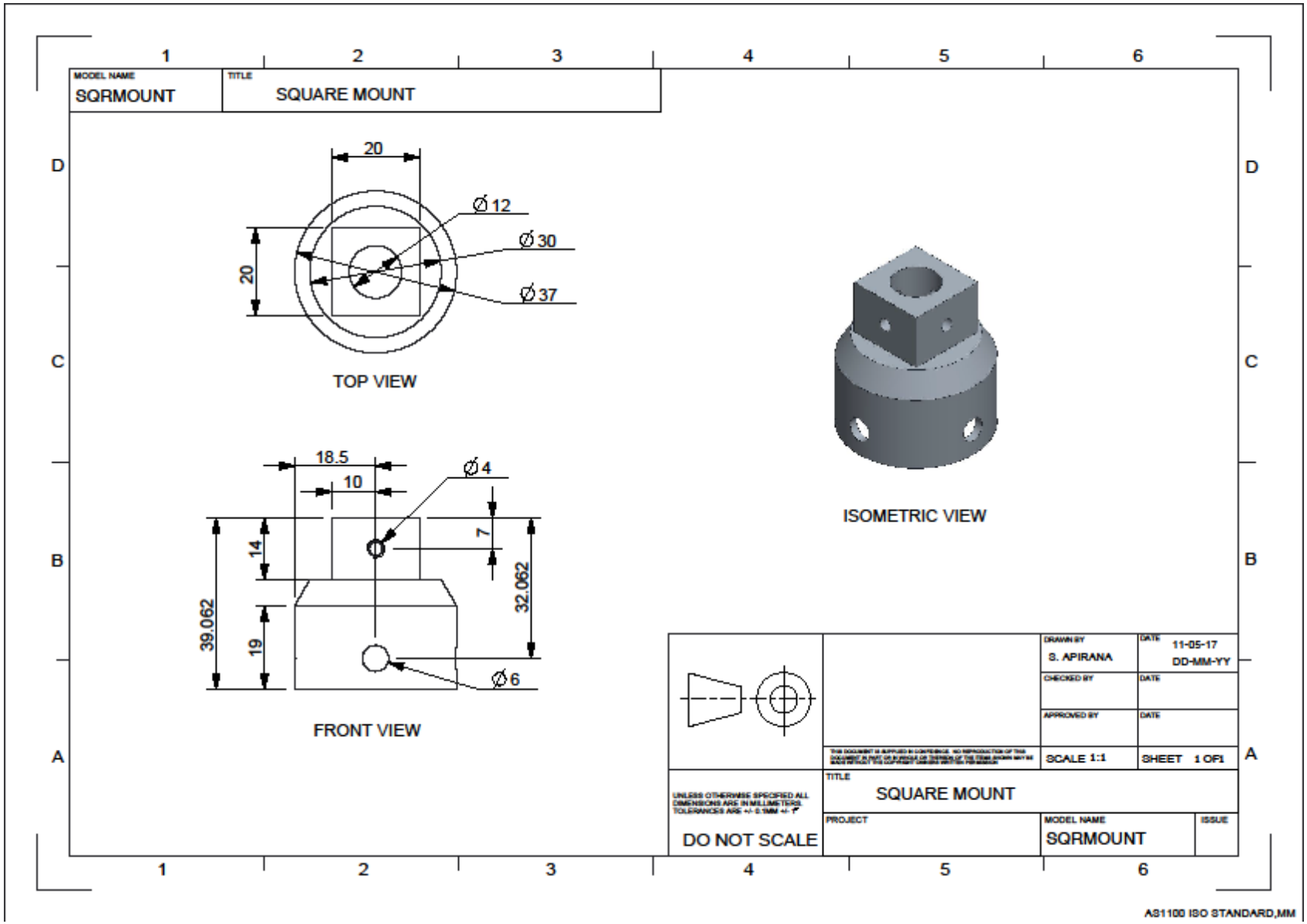

MODEL NAME	TITLE
STING	STING

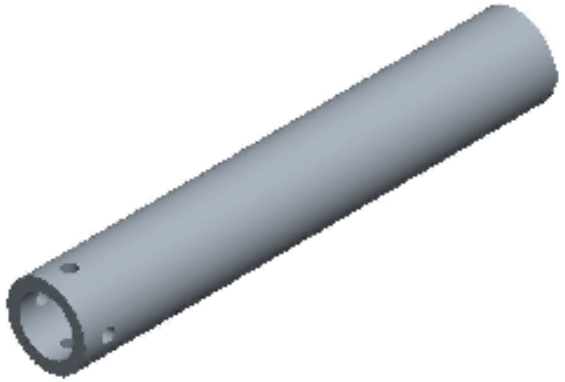

ISOMETRIC VIEW

FRONT VIEW

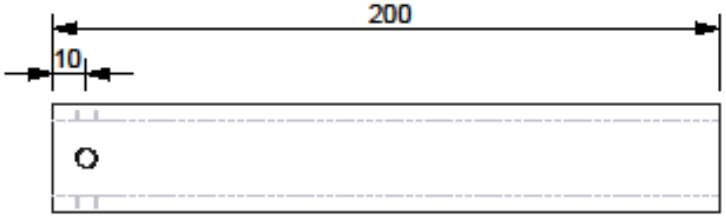

SIDE VEIW

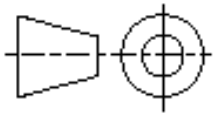

		DRAWN BY: S.APIRANA	DATE: 11-05-17 DD-MM-YY
		CHECKED BY	DATE
		APPROVED BY	DATE
	THIS DOCUMENT IS SUPPLIED IN CONFIDENCE. NO REPRODUCTION OF THIS DOCUMENT IN PART OR IN WHOLE OR DISPLAY OF THE ITEMS SHOWN MAY BE MADE WITHOUT THE EXPRESS PERMISSION OF THE OWNER.	SCALE 1:2	SHEET 1 OF1
UNLESS OTHERWISE SPECIFIED ALL DIMENSIONS ARE IN MILLIMETERS TOLERANCES ARE +/- 0.1MM +/- 1° DO NOT SCALE	TITLE: STING		
	PROJECT	MODEL NAME: STING	ISSUE

AS1100 ISO STANDARD,MM

MODEL NAME	TITLE
LOWER	LOWER CUBESAT

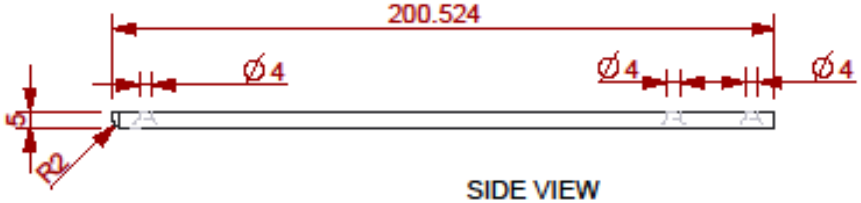

SIDE VIEW

ISOMETRIC VIEW

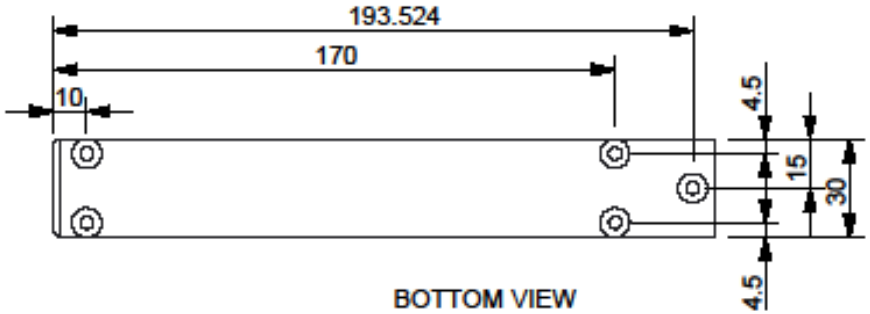

BOTTOM VIEW

		DRAWN BY: S.APIRANA	DATE: 11-05-17 DD-MM-YY
		CHECKED BY	DATE
		APPROVED BY	DATE
	THIS DOCUMENT IS SUPPLIED IN CONFIDENCE. NO REPRODUCTION OF THIS DOCUMENT IN PART OR IN WHOLE OR TRANSFER OF THE ITEMS SHOWN MAY BE MADE WITHOUT THE COMPANY'S PRIOR WRITTEN PERMISSION.	SCALE 1:2	SHEET 1 OF1
UNLESS OTHERWISE SPECIFIED ALL DIMENSIONS ARE IN MILLIMETERS. TOLERANCES ARE +/- 0.1MM +/- 1°	TITLE: LOWER CUBESAT		
DO NOT SCALE	PROJECT	MODEL NAME: LOWER	ISSUE

AS1100 ISO STANDARD,MM

MODEL NAME	TITLE
UPPER	UPPER CUBESAT

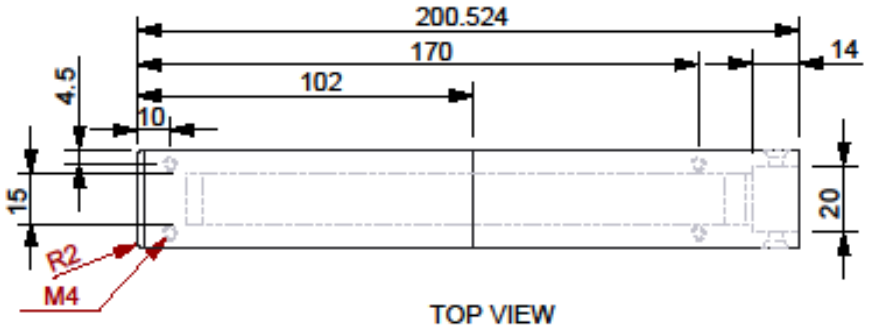

TOP VIEW

ISOMETRIC VIEW

RECESS USED TO HOUSE INSTRUMENTS.
INNER EDGE FINISHES AND RADII CAN
BE VARIED FOR EASE OF MACHINING.

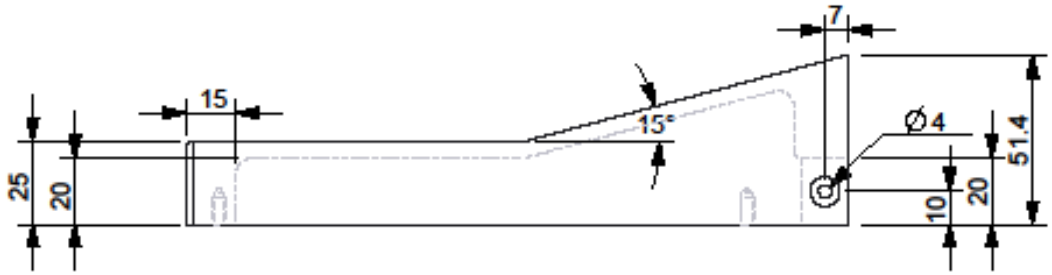

SIDE VIEW

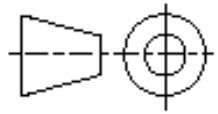

		DRAWN BY: S.APIRANA	DATE: 11-05-17 DD-MM-YY
		CHECKED BY	DATE
		APPROVED BY	DATE
	THIS DOCUMENT IS SUPPLIED IN CONFIDENCE. NO REPRODUCTION OF THIS DOCUMENT IN PART OR IN WHOLE OR DISTRIBUTION OF THE ITEM SHOWN MAY BE MADE WITHOUT THE COPYRIGHT OWNERS WRITTEN PERMISSION	SCALE 1:2	SHEET 1 OF1
UNLESS OTHERWISE SPECIFIED ALL DIMENSIONS ARE IN MILLIMETERS TOLERANCES ARE +/- 0.1MM +/- 1°	TITLE: UPPER CUBESAT		
DO NOT SCALE	PROJECT	MODEL NAME: UPPER	ISSUE

AS1100 ISO STANDARD,MM

MODEL NAME	TITLE
MOUNTEDASSEMBLY	MOUNTED ASSEMBLY

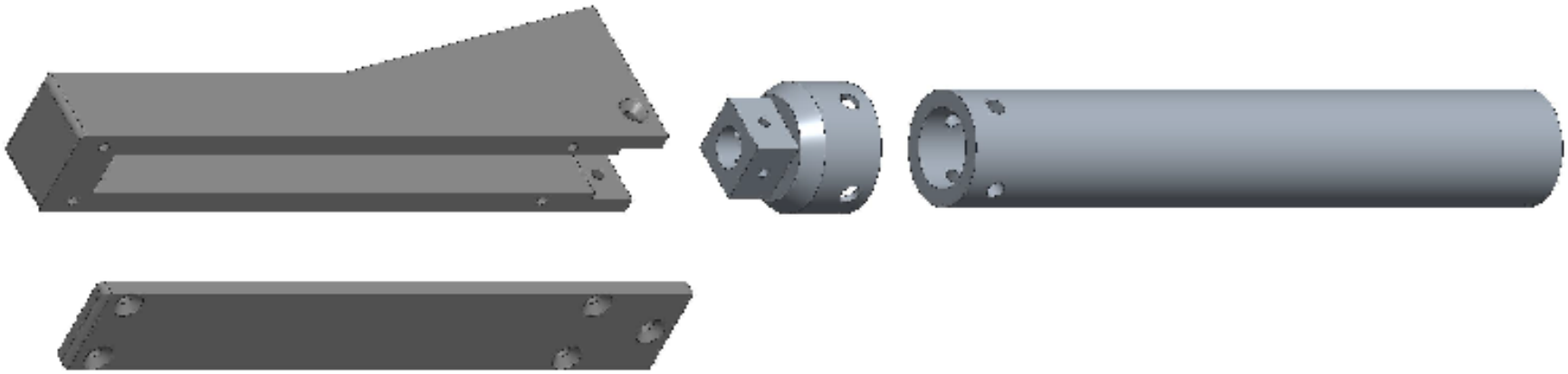

EXPLODED VIEW

		DRAWN BY: S.APIRANA	DATE: 11-05-17 DD-MM-YY
		CHECKED BY	DATE
		APPROVED BY	DATE
	THIS DOCUMENT IS SUPPLIED IN CONFIDENCE. NO REPRODUCTION OF THIS DOCUMENT IN PART OR IN WHOLE OR DETAIL OF THE ITEM SHOWN MAY BE MADE WITHOUT THE COPYRIGHT OWNERS WRITTEN PERMISSION	SCALE 3:5	SHEET 1 OF1
UNLESS OTHERWISE SPECIFIED ALL DIMENSIONS ARE IN MILLIMETERS TOLERANCES ARE +/- 0.1MM +/- 1°	TITLE: MOUNTED ASSEMBLY		
DO NOT SCALE	PROJECT	MODEL NAME: MOUNTEDASSEMBLY	ISSUE

AS1100 ISO STANDARD,MM